CHAPTER 3

Particle Image Velocimetry Techniques and its Applications in Multiphase Systems

Feng-Chen Li[1] and **Koichi Hishida**[2,*]

Contents

1 School of Energy Science and Engineering, Harbin Institute of Technology, Harbin 150001, China

2 Department of System Design Engineering, Keio University, Yokohama 223-8522, Japan

*Corresponding author
E-mail address: hishida@sd.keio.ac.jp

Advances in Chemical Engineering, Volume 37
ISSN: 0065-2377, DOI 10.1016/S0065-2377(09)03703-X

Abstract

This chapter is devoted to the methodology of particle image velocimetry (PIV) techniques and its applications to multiphase flow systems. It reviews, first, the fundamental issues of a conventional PIV with considerations of improvements of spatial resolution and accuracy; second, the state of the art in various types of PIV techniques from the viewpoint of dimensions and velocity components of the measurement, the flow passage scales, and the hardware components of the system; third, the state of the art in some issues about the measurement of multiphase flow systems using PIV techniques. The multiphase flows to which the applications of PIV techniques are discussed include liquid–liquid two fluid flows, gas–liquid two-phase flows, and particle-laden multiphase flow systems.

The emphasis in this chapter is on the fruitful methodology of PIV techniques that emerge in the recent publications instead of the detailed discussions on any individual research topic of the measurement target of PIV. The purpose is to provide an overall instructive introduction and guidance to the PIV techniques and its applications particularly in the research field of multiphase flows. To this end, fruitful examples of PIV measurements of free-surface liquid flows, bubbly flows, particle-laden multiphase flows, etc., are elucidated.

1. INTRODUCTION

Particle image velocimetry (PIV) is one of the nonintrusive flow diagnostics tools, which provide quantitative measurements with high spatial and high temporal resolution of whole field velocity profiles in liquids, gases, multiphase flows, and even the fluid-like flows of solid particles or granular flows. Since its invention for more than two decades, PIV, as a nonintrusive, accurate, reliable, convenient, and very powerful experimental technique for flow diagnostics, has been playing a highly important role in the fundamental studies on fluid dynamics, a wide range of industrial applications, understanding a variety of natural phenomena, and even exploring some flow characteristics in the body of human beings. The widely demonstrated applications of PIV technique may range from very low speed flows to supersonic flows (e.g., Ganapathisubramani et al., 2006a; Ganapathisubramani, 2007), from flows in a nano/micro-scaled passage to flows at a large scale as a river (e.g., Ettema et al., 1997), from single-phase to multiphase flows, from nonreactive flows to reactive flows as combustion, from cryogenic (e.g., Van Sciver et al., 2007; Harada et al., 2006; Zhang and Van Sciver, 2005) to very high temperature flows (e.g., Balakumar and Adrian, 2004), and from inanimate flows to flows around living beings (e.g., Stamhuis, 2006).

For summarization of the development of PIV, there have timely appeared many volumes of books or monographs or pieces of review papers on the topic (e.g., Adrian, 1991; Raffel et al., 2007; Westerweel, 1997, among others), which have well-documented the PIV technique in common senses.

In lieu of its great importance, widely spreading communities of PIV techniques, including the development of PIV and application of PIV, have emerged all over the world. There are always a large part of participations giving presentations of PIV techniques to the relevant international conferences or symposiums or subsessions of them. Sought from the "ISI Web of Knowledge" (http://apps.isiknowledge.com) using the keyword of PIV or its full spelling, it can be seen that the number of published papers about PIV in the peer-reviewed journals increases more than 10 times from 39 papers in the year of 1994 to 464 papers in 2007, as shown in Figure 1. If sought from "Google" website, the number of PIV issues, which include journal papers, conference papers, and other issues, is from 263 items in 1994 to 2270 items in 2007. After the continuously increasing development and application, the PIV techniques have partly become one of the standard diagnostics tools of flow measurement. Nevertheless, PIVs are still partly under development such as the holographic micro-scaled PIV technique for three-dimensional (3D) flow measurement in microchannels.

Multiphase flow systems appear almost everywhere in the world, including the natural phenomena, industrial applications, and daily life of human beings. The application of PIV techniques to multiphase flow measurement has also been flourished. Among the flow measurement

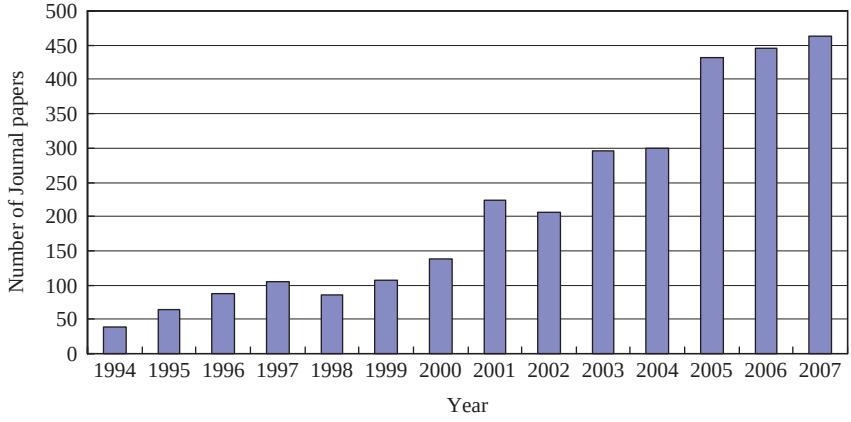

Figure 1 A survey of the number of published journal papers about development or application of PIV technique from 1994 to 2007 based on the database from "ISI Web of Knowledge" (http://apps.isiknowledge.com).

using PIV techniques, multiphase flows may have taken the most complex and difficult supplemental considerations to the experimentalists. The complexity emerges from that the multiphase systems usually involve a variety of operating modes of gas, liquid, and solid phases, including those with solid particles and liquid droplets in dispersed states, which will severely influence a normal PIV measurement without any particular treatment. The summarization of PIV techniques used for flow measurement of multiphase systems is, however, relatively scarce compared with those of PIV technique in common senses.

This chapter is therefore intended to describe the fundamental issues on PIV technique in brief, the versatility of PIV techniques from the viewpoint of its hardware components as well as the resolved dimensions. The chapter is also intended to discuss the state of the art in the special PIV techniques (sometime with the aid of other supplementary technique) applied to the measurement of multiphase flows. Note that, the emphasis in this chapter is on the methodology of PIV techniques instead of details of the individual study on any research topic.

2. FUNDAMENTALS OF PARTICLE IMAGE VELOCIMETRY

The principle of conventional two-dimensional (2D) digital PIV technique is to illuminate (for transparent flow media) a particle-seeded flow field with two laser sheet pulses separated by a time delay and capture the image of the particles with a charge-coupled device (CCD) camera. The captured images are then subdivided into an array of small size interrogation windows. In each interrogation window, all particles are assumed to have essentially the same velocity. The overall displacement of particles within each interrogation window is then calculated with a numerical correlation algorithm. Finally, the velocity vectors of the whole illuminated flow field are obtained with dividing the displacement by the time delay between the illuminating laser sheet pulses. For any kind of fluid flow that is transparent to enable imaging of the seeded particles mixed in the fluid, including gas flow, liquid flow, gas–liquid two-phase flow, and gas–liquid–solid three-phase flow, PIV can be applied to measure the whole field velocity distribution. A generalized PIV setup is shown in Figure 2. Apart from this kind of conventional PIV, that is, pulsed lasers, particle seeding, and transparency of the flow media are required, imaging procedure and velocity derivation algorithm of PIV technique has been applied to develop measurement approaches for the flow velocity distribution at the surface of some kind of fluid-like flow or opaque fluid flow, such as granular flow (e.g., Deng and Wang, 2003; Lueptow et al., 2000; Ostendorf and

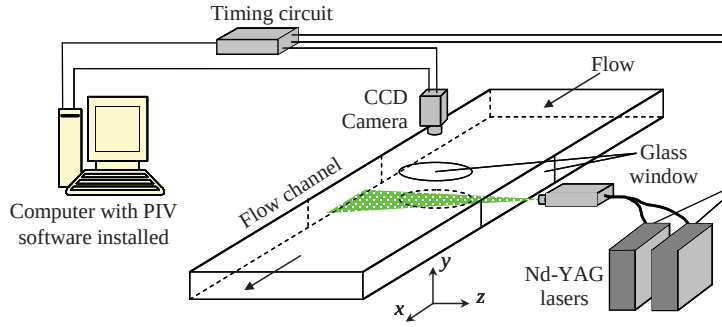

Figure 2 Diagram of a generalized 2D-PIV setup showing all major components: flow channel with the particle seeded fluid flow, laser sheet pulses illuminating one plane in the fluid, a CCD camera imaging the particles in the laser-illuminated sheet in the area of interest, a computer with PIV software installed, a timing circuit communicating with the camera and computer and generating pulses to control the double-pulsed laser. The PIV software setups and controls the major components, and analyses the images to derive a vector representation of flow field (see Plate 4 in Color Plate Section at the end of this book).

Schwedes, 2005; Sielamowicz et al., 2005; Steingart and Evans, 2005; Zhao et al., 2008), ice flow floating at the surface of a river (e.g., Ettema et al., 1997) and so on. In those cases, not all of pulsed lasers, particle seeding, and transparency of the flow are necessary. The following fundamental descriptions are based on a conventional 2D digital PIV technique. For other kinds of PIV, the principles and analysis algorithms are straightforward, which will be individually briefed in the next section.

2.1 Seeding the flow

To visualize the flow for PIV purposes, the measured fluid flow has to be seeded with particles, which need to be neutrally buoyant and small with respect to the flow phenomena studied (e.g., Raffel et al., 2007). For different sorts of visualized flow, seeding particles could be quite different.

For liquid flows, a series of polymer powders or particulate half-products for plastics with a range of densities are available and can be matched to the fluid density. In water flow for example, polystyrene, polythene, nylon, pliolite particles work well and are commercially produced in a range of diameters typically from 5 to 200 μm. Seeding gas flows, particularly at low speed, might be more difficult than seeding water flow, since particles tend to sink due to its relatively high density compared with that of gas. The seeding particles thus need to be very light and small, for example, very small polystyrene beads with diameter of 5–10 μm (Stamhuis, 2006 among others). In high speed air flow, for

example, in a wind tunnel flow, water droplets or vegetable oil produced with an aerosol generator in diameters of 1–10 μm are commonly used (Raffel et al., 2007). Melling (1997) comprehensively stressed the issues on tracer particles and seeding for PIV, including the size specifications for suitable tracer particles particularly with respect to their flow tracking capability, a wide variety of tracer materials used in liquid and gases, and methods of generating seeding particles and introducing the particles into the gas flows.

In the gas–liquid two-phase flows illuminated by a laser sheet, for example, the intensity of light reflected from the gas–liquid interface (mostly the gas bubble's surface) not only saturate the CCD camera, but also overwhelm the intensity of light from the seeded tracer particles in its vicinity. Fluorescent particles are often used to realize the laser-induced fluorescence (LIF) technique together with PIV (e.g., Broder and Sommerfeld, 2002; Fujiwara et al., 2004a, b; Kitagawa et al., 2005; Liu et al., 2005; Tokuhiro et al., 1998, 1999), so that both images of gas–liquid interface (e.g., bubble's geometry) and velocity distribution in the liquid phase around the gas bubbles can be obtained. Issues on PIV measurement of gas–liquid two-phase flows will be further illustrated in the latter sections.

A summarization of different seeding particles for the PIV measurement of water and air flows, which are the most often encountered, is provided in Table 1.

2.2 Illumination and image recording

A laser light sheet is usually adopted for the illumination in PIV flow studies, since it may have strong enough brightness and almost constant thickness without aberration or diffusion due to the coherent and monochromatic character of the emitted laser light. Some exceptions, such as the conventional microscopic PIV (μ-PIV), PIV technique for granular flows and so on, will be mentioned in the later relative sections. The slightly diverging light beam produced by a laser is usually transformed into a sheet by converging it with a weak positive lens and subsequently making the beam fan out in one plane to a sheet by an additional cylindrical lens. This results in a sheet with a lightly converging thickness, enabling one to select a certain sheet thickness tuned to the certain experimental conditions. The minimum thickness of the laser sheet locates at the focal point of the outermost convex lens of the optics and is calculated with the following equation when the Rayleigh length of the light sheet is much larger than the focal length of the lens: $\delta_m = 4F\lambda/\pi d_0$, where F is the focal length of the convex lens, λ the laser wave length, and d_0 the diameter of the laser beam.

Table 1 The often used seeding particles for PIV measurement of water and air flows

For water flow			For gas flow		
Type	Material	Diameter (μm)	Type	Material	Diameter (μm)
Solid	Polystyrene	10–100	Solid	Polystyrene	0.5–10
	Polymer fluorescent microspheres	0.1–1		Alumina Al_2O_3	0.2–5
	Glass spheres	10–100		Magnesium	2–5
	Hollow glass spheres	10–150		Titania TiO_2	0.1–5
	Hollow plastic spheres	10–50		Glass microspheres	0.2–3
	Aluminum flakes	2–7		Hollow glass spheres	10–100
	Granular particles with coating	10–500		Hollow plastic spheres	10–50
	Ion exchange resin	30–700		Granular particles with coating	10–50
Liquid	Oils	50–500		Ion exchange resin	1–30
Gas	Oxygen bubbles	50–1,000		Smoke	<1
			Liquid	Oils	0.5–10
				Water	0.5–10

For a two-dimensional two-component (2D-2C) PIV measurement, the main flow direction and the laser light sheet for illumination generally have to be aligned, otherwise the out-of-plane problem of the illuminated particles, that is, the particles illuminated and pictured in the first image disappear from the illuminated plane and being replaced by others in the second image, resulting in the loss of coherence of the two images, could be serious.

Two types of lasers are commonly used for PIV illumination: continuously emitting laser also named continuous wave (CW) lasers and pulsating lasers. Pulsed lasers, for example, Nd:YAG lasers, can produce power light with high energy per pulse with very short intervals between two pulses. For a high-speed flow to be studied, pulsed lasers are therefore highly recommended, since short illumination times and a high pulse frequency are usually necessary to image the particles seeded in the flow. For a standard 2D-2C PIV, two pulsed lasers such as Nd:YAG lasers are used. The CW laser, for example, He–Ne laser or Ar laser, produces relatively low power light of good beam quality within a short interval. Pulsed lasers, like Nd:YAG lasers, are usually more expensive and more difficult to set up due to the added timing and synchronization equipment compared with CW lasers. In some particular cases, such as PIV studies of liquid Helium (e.g., Van Sciver et al., 2007; Zhang et al., 2004; Zhang and Van Sciver, 2005), CW lasers are less desirable as they provide a steady background heat loading to the experiment. Instead, short pulse Nd:YAG solid-state lasers operating at minimum power are effective.

For 2D-2C PIV measurement, the illuminated plane in which seeded particles to the flow should be clearly visible and homogeneously distributed, is imaged by a camera with its optical axis perpendicular to the plane. High quality lenses are generally acquired because the light powers are usually not very strong and large apertures have to be used. The up-to-date PIV commonly uses electronic cameras with a CCD or complementary metal-oxide semiconductor (CMOS) pick-up device. Electronic cameras are available in a whole range of resolutions, sensitivities, shutter speeds, and frame rates. For a certain flow to be studied, such as a turbulent flow with highly frequent events, repeatability, and illumination intensity need to be evaluated for choosing a suitable camera often in combination with the illumination system. Most of the electronic camera used for PIV are available with sensor resolutions of 512×512 pixels or $1\,\mathrm{K} \times 1\,\mathrm{K}$ pixels or higher. The frame rate of electronic cameras for PIV system can range from 25 to 30 fps, which is for the normal PIV, to 1,000 fps at full sensor resolution and much higher rates at reduced image sizes, which is for the time-resolved or dynamic PIV (e.g., Bi et al., 2003; Fore et al., 2005; Li et al., 2007; Triep et al., 2005). Dynamic PIV can be used for flow analysis,

enabling mapping of unique flow velocity distributions in both space and time.

A double-exposure electronic camera is capable of recording two frames within a very short inter-frame interval and transferring both frames to the host system, and then the camera is prepared for the next image pair. Depending on the purpose, such as for measuring high speed repeatable flow events or only taking snap-shots of a flow, adjustment of the inter-frame times of double-exposure cameras can be conducted from 0.5 μs to even 0.5 s (Raffel et al., 2007; Stamhuis, 2006). On the other hand, a double-exposure camera has to be used in combination with a pulsed laser due to the construction of the camera shutting system. In addition to the combination of a double-exposure camera with pulsed lasers, a continuous video stream and a CW laser together with an external fast shutter could be a low-cost alternative for PIV application. The shuttering may result in relatively low illumination levels, which usually requires a more powerful CW laser.

2.3 PIV analysis

Figure 3a shows an example of the image pair taken by PIV cameras. Dense particle images are clearly visible in the pictures. It is not possible to measure the displacement of each tracer particle separately. Therefore, each of the frames is divided into small square areas named interrogation windows (Figure 3b). The size of the interrogation windows depends on the desired accuracy, the resolution of the measurement and the quality of the image recording. Typically, an unambiguous result for the particle-image displacement can be obtained from a minimum of 3–4 particle images using a correlation analysis. Keane and Adrian (1992) analyzed that the probability for a good analysis result is highest when the interrogation window contains approximately 8–10 particle images. Correlation analysis is then performed to find the displacement peak, by which the average displacement of the particles within each interrogation window is abstracted and the velocity vector is calculated. Repeating the procedures, the velocity distribution in the whole field of the PIV image is then obtained.

With the technological growth and performance improvement of digital cameras, digital cross-correlation methods are now almost generalized for analyzing recorded PIV images (Willert and Gharib, 1991). Cross-correlation removes the autocorrelation peak and directional ambiguity (i.e., there is only one peak) which are present in autocorrelation algorithm at the early stage of the development of PIV. Hence, only the issues related to cross-correlation approach of PIV are briefed as follows.

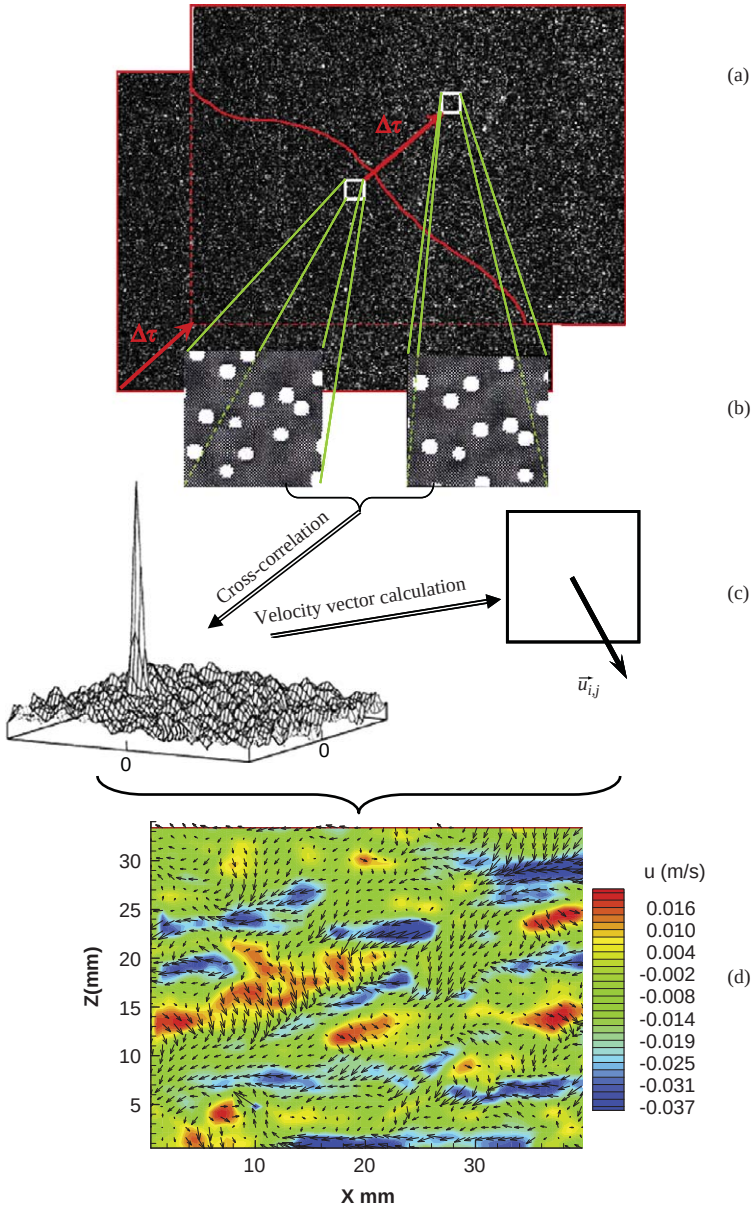

Figure 3 Diagram of the steps in PIV analysis of successively recorded particle images in a flow: (a) two successive PIV images; (b) two subimages called interrogation window from the same location of two frames; (c) a dominant peak of the cross-correlation calculation representing the most probable average displacement of particles containing in the interrogation window and through which the velocity vector is calculated; and (d) a whole field 2D velocity field obtained from the pair of PIV image.

2.3.1 Cross-correlation analysis for PIV

Traditional forms of digital PIV analysis algorithms have relied on autocorrelation and cross-correlation schemes. Cross-correlation implementations are typically favored over autocorrelation approaches since the former yielded directionally unambiguous displacements and have been found to provide more robust and superior performance, for example, lower correlation noise, larger dynamic range (the maximum velocity range that can be measured with a fixed set of instrumental parameters divided by the minimum resolvable velocity measurement; Adrian, 1997), and less gradient bias (Keane and Adrian, 1992; McKenna and McGillis, 2002). Supposing an interrogation window with size of $N \times N$ pixel, the discrete cross-correlation function is written as $c_{fg}(\Delta x, \Delta y) = \sum_{i=1}^{N} \sum_{j=1}^{N} f(x_i, y_j) g(x_i + \Delta x, y_j + \Delta y)$, where f and g are the variables (e.g., intensity values) extracted from both the images, (x_i, y_j) is the current position of calculation, and $(\Delta x, \Delta y)$ the sample shift. The normalized cross-correlation, that is, cross-correlation coefficient given by the following equation, is often used:

$$R_{fg}(\Delta x, \Delta y) = \frac{\sum_{i=1}^{N} \sum_{j=1}^{N} \left\{ f(x_i, y_j) - f_m \right\} g\left\{ (x_i + \Delta x, y_j + \Delta y) - g_m \right\}}{\sqrt{\sum_{i=1}^{N} \sum_{j=1}^{N} \left\{ f(x_i, y_j) - f_m \right\}^2 \sum_{i=1}^{N} \sum_{j=1}^{N} g\left\{ (x_i + \Delta x, y_j + \Delta y) - g_m \right\}^2}}$$

where f_m and g_m are the average values within the $N \times N$ pixel subareas in both PIV images, respectively. Early PIV cross-correlation analyses were performed in the Fourier domain, as this provided the most efficient means of processing the data (e.g., McKenna and McGillis, 2002; Willert and Gharib, 1991). With the development of faster computer CPUs, the need for transformation into frequency space is becoming less imperative and some methods of correlation are performed mandatorily in the spatial domain directly.

To get the most probable displacement of the particle pattern in the interrogation window, a mathematical correlation procedure is applied. One can imagine this procedure as "moving window 1 over window 2 until the best matching is found." "Best matching" is used here since in practice 100% matching can never be reached due to particles that have left or entered the interrogation window in the second image compared with the first. Mathematically, there are two methods used for image correlation analysis: Fourier transformations and convolution filtering. The results of both algorithms are comparable. Details on the mathematics of both methods have been well documented (e.g., Raffel et al. 2007).

Performance of cross-correlation leads to the correlation plane as seen in Figure 3c, which depicts the correlations versus the displacement in x

and y direction of a 2D coordinate system. Figure 3c shows a typical result of the calculation of the cross-correlation, with many small peaks and only one dominant peak. The displacement that belongs to this dominant peak is the most probable displacement because the dominant peak indicates the ''best matching'' of particle images between the two interrogation windows. With the abstracted most probable displacement, the (mean) velocity vector of the interrogated subimage area is then calculated by dividing the time interval between the two investigated PIV images, $\Delta\tau$, and is usually located at the center of the present interrogation window (Figure 3c). Repeating the preceding procedures, a whole field 2D velocity distribution is yielded finally (Figure 3d).

2.3.2 Resolution improvement

Spatial resolution is one of the most important points of the performance of a PIV system. For conventional correlation analysis of PIV, the spatial resolution is bounded by the size of the measurement volume, which is determined by the intersection of the illuminated light sheet with the interrogation window density distribution (Keane et al, 1995). In contrast with the limiting role of the interrogation window size in the resolution of conventional correlation PIV methods, an iterative multipass correlation PIV analysis approach is developed and elaborated by Nogueira et al. (1999, 2001a, b, 2005a, b), which yields resolutions below the window size using a particular weighting function (Huang et al., 1993; Jambunathan et al., 1995). The multigrid analysis obtained by progressively refining the interrogation window size and deformation during iterative interrogation is proved to increase the accuracy as well as spatial resolution of the PIV technique (Fincham and Delerce, 2000; Scarano and Riethmuller, 2000; Theunissen et al., 2007). Several well-documented approaches for improving spatial resolution are briefed as follows.

Particle tracking velocimetry (PTV) algorithms are based on the tracking of individual particle images and allow in principle the highest spatial resolution, that is, one vector for each detected particle (Keane et al., 1995; Theunissen et al., 2007). The super-resolution approach is then developed, which incorporates conventional cross-correlation PIV followed by subgrid particle tracking within the interrogation window (Bastiaans et al., 2002; Keane et al., 1995; Stitou and Riethmuller, 2001; Susset et al., 2006). The essence of this method is to enhance particle tracking by means of the PIV information. The technique is a hybrid algorithm that starts by statistical evaluation of a tracer's displacement (PIV correlation) and further refines the resolution of measurement with the tracking of individual particles (PTV) within the interrogation window. This technique improves not only the spatial resolution but also the accuracy. The velocity field obtained is unstructured due to the random position of the particles inside the flow field. For more convenience,

for example, to compare with other databases or data analysis in a structured form, a data redistribution method can be applied on a structured grid.

Window displacement iterative multigrid (WIDIM) interrogation method has been proposed and developed to improve the resolution for PIV (Fincham and Delerce, 2000; Scarano, 2002, 2004; Scarano and Riethmuller, 1999, 2000; Soria, 1996; Theunissen et al., 2007). The essence of WIDIM is to compensate for the loss-of-pairs of particles due to in-plane motion. To do this, the local displacement of each interrogation window is made on the basis of a flow pattern prediction. The predicted displacement is obtained by a previous interrogation of the set of two PIV images, therefore, it is necessary to adopt an iterative procedure (Scarano and Riethmuller, 1999). At the start of the process, no *a priori* information on the flow pattern is available and the first predictor is set uniformly to zero. After the first interrogation, the coarse result will be used as a predictor. A finer windowing is then made halving the windows in both directions and the predictor is applied to the window offset by means of simple substitution of the previous iteration result. As a consequence, in the subsequent steps, the one quarter rule (Raffel et al., 2007) related to the in-plane displacement does not limit anymore the size of the windows and the PIV images can then be interrogated with a better resolution. Involving similar consideration, Hart (2000a) achieved an increased spatial resolution by recursively correlating the image frames at finer grid sizes down to the size of an individual particle image. Correlation search length is also reduced iteratively to the smallest meaningful scale parallel with the decrease of interrogation window size.

Local-field correlation particle image velocimetry (LFCPIV) is another method to resolve flow structure smaller than the interrogation window size (Nogueira et al., 1999, 2001a, 2005a, b). It is also said that LFCPIV is the only correlation PIV method being able to yield super resolution (Nogueira et al., 2001a). The interrogation windows for LFCPIV are fixed in size and location. After each iteration step, however, the image is redefined through compensation of the particle pattern deformation caused by the velocity gradient in the flow field. This implies both displacement and deformation of the image. It is performed using the displacement field from the previous evaluation. As a result, this method presents the ability to resolve small structures with large interrogation windows. In LFCPIV, a proper weighting function is defined to avoid the instability related to high spatial frequency. The combination of the two capabilities, that is, the ability to cope with large velocity gradients and to resolve small structures in the flow, results in a very robust high-resolution technique (Nogueira et al., 2001a, b).

There are also several other alternatives to resolution improvement methods for PIV, such as hierarchical processing method, reverse hierarchical processing method and so on. For those, one can refer to the relative references (Kumar and Banerjee, 1998; Rohaly et al., 2002; Susset et al., 2006; Westerweel et al., 1997, among others).

2.3.3 Inherent error elimination and accuracy improvement

The accuracy of PIV measurement (before post-processing) depends on several factors, including the properties of target flow fields, the properties and concentration of seeding particles, the optical setup, the data acquisition system, the image interrogation technique, etc. (Chen and Katz, 2005). Among them, the error introduced during image interrogation has received the most attention since it provides the widest latitude for development of optimization tools (Chen and Katz, 2005; Huang et al., 1997; Huang, 1998; Keane and Adrian, 1990; Lecordier et al., 2001; Westerweel, 1997). The uncertainties associated with PIV measurements can be classified into two categories: random error and bias error. The random errors in PIV are most often associated with electronic noise in the cameras, shot noise, and random errors associated with properly identifying the subpixel displacement (Christensen, 2004). Owing to its random nature, the influence of random errors can be reduced by statistical analysis using a sufficiently large ensemble set. Bias errors are not random in space and time and can degrade not only the accuracy of instantaneous PIV results, but also any statistic computed from biased PIV ensembles. Several bias errors can exist in a PIV measurement, including uncertainties associated with the fill ratio of the CCD camera and the algorithm used to interrogate the images (Christensen, 2004). The most significant bias error is the so-called peak-locking error (e.g., Christensen, 2004; Fincham and Spedding, 1997; Hart, 2000b; Raffel et al., 2007), that is, the biasing of particle displacements toward integer pixel values, which inherently stems from the choice of subpixel finding algorithm, underresolved optical sampling of the particle images, and the truncation of particle images by the borders of the interrogation window (Nogueira et al., 2001a). Here, some of the techniques coping with the peak-locking error are summarized briefly as follows.

As mentioned previously, the location of the peak in the cross-correlation plane of a pair of interrogation windows yields the mean particle displacement within the first window. To achieve subpixel accuracy, a smooth curve is typically fitted through 3–4 points in the vicinity of the discrete correlation peak. This subpixel curve fitting causes a bias toward discrete values of displacement (i.e., peak-locking error). To remedy or eliminate the peak-locking effect, several methods have been proposed. Westerweel (1997) proved that a Gaussian subpixel estimator is superior to both centroid and quadratic fits in terms of

mitigating peak-locking effects. A *Sinc* function is recommended by Roesgen (2003) to suppress the spurious spectral side lobes in the correlation resulting in minimal peak-locking effects for adequately resolved particle images. On the basis of the fact that there should be no bias error when the true displacement is an integer pixel, a solution to reduce peak-locking is to apply the continuous window shifting technique (Gui and Merzkirch, 2000; Gui and Wereley, 2002; Liao and Cowen, 2005; Nogueira et al., 2001a), that is, iteratively shift the interrogation window by fractional displacements until the final determined subpixel displacement is driven to zero.

Since the peak-locking error is due to the subpixel curve fitting, more advanced error-elimination methods have been proposed by bypassing the subpixel curve fitting. Fincham and Delerce (2000) developed a peak anti-aliasing, spline transformed interrogation scheme involving interpolation of pixel values but without involving subpixel fitting to the correlations. Chen and Katz (2005) proposed a correlation mapping method to eliminate the peak-locking error in PIV analysis, which bypasses the subpixel curve fitting and so eliminates the peak-locking effect, but does not require iterations as the continuous window shifting technique does. Using subpixel interpolation, this method expresses the second exposure of an interrogation window as a polynomial function with unknown displacement, whose coefficients are determined by the grayscale distribution of the first image (Chen and Katz, 2005). Thus, the correlation between this function and the first exposure is also a polynomial of the displacement. This virtual correlation function can be matched with the exact correlation value at every point in the correlation map. A least-squares method is used to find the optimal displacement components that minimize the difference between the real and virtual correlation values in an (e.g., 5×5 pixel) area surrounding the discrete correlation peak. The correlation mapping method returns superior results compared to the Gaussian subpixel interpolation.

2.4 Post-processing of velocity vectors

The resultant velocity vector set of automated PIV analysis often includes a certain number of incorrect vectors that are usually obvious in the vector diagram. Such spurious vectors are usually due to imperfections in the input PIV images, caused by local variations in seeding density, local over-illumination due to an object or wall in the light sheet, strong out-of-plane flow, local low illumination close to the image borders, or crippled interrogation windows next to the image border. These problems cause lack of correlation in the normal way, and a background (noise) peak is then recognized as if it were the displacement peak, resulting in a spurious vector.

Elimination of the spurious vectors is usually performed by comparing them with their neighbors. Errors are recognized if they are inconsistent with neighbors in some statistical or physical sense. False vectors can also be identified by the ensemble method, in which outliers are removed from the ensemble-averaged velocity field based on the standard deviation of the velocity at each grid (Wernet, 2000). The simplest and commonly used post-processing technique is the local-median method. The median is the middle value (nth element) of a sequence of $2n+1$ scalar elements (Westerweel, 1994), that has been rearranged in increasing or decreasing order (for even number of elements, the median is equal to the mean of the two middle elements). Westerweel (1994) showed that the local-median method is more efficient than the global- and local-mean methods. The local-median method with constant user-adjustable thresholds is usually adequate to detect the spurious vectors when a proper threshold is set for a specified flow field. However, a single constant threshold is generally not applicable in complicated flows such as inhomogeneous gradient flows or vortical flows. For this, Liu et al. (2008) proposed a flow-adaptive data validation scheme to avoid the selection of the appropriate thresholds for specified flow fields, which shows superior performance to the local-median method.

Once the false or spurious vectors are recognized and removed, empty grids should be filled by new vectors, which should be representative of the local flow velocity as close as possible, for continuous calculation of local derivatives and gradient parameters. To do this, 2D interpolation is commonly performed. Although simple linear or polynomial interpolation can obtain reasonable results, the best and also principally the most reliable results have been yielded with 2D cubic natural spline interpolation (Spedding and Rignot, 1993). Cubic natural spline fits leave the original neighboring data unaffected and find the missing points according to ''the most fluent line or plane,'' that is, with minimization of the local curvature. This algorithm works well for shock waves in transonic flow as well as in a noncompressible or subsonic compressible fluid flows. In some cases more often than not, spurious vectors may still exist in a PIV measured 2D velocity field after performing data-validation procedures with any methods. Afanasyev and Demirov (2005), thus, designed a variational filtration and interpolation technique to reduce the effect of spurious vectors, which cannot be removed by other methods or to reconstruct the velocity field in the areas where the outliers are removed. This method is based on the application of dynamical constraints such as continuity, smoothness, and matching to the original data, rather than a simple statistical approach. After the treatment of spurious vectors, that is, detection, elimination, and filling the holes, final analysis of the acceptable velocity vectors can be finally conducted with physical meaning.

3. VARIOUS TYPES OF PARTICLE IMAGE VELOCIMETRY

At the very early stage, the light scattered by the tracer particles for a PIV system is recorded via a high quality lens on a film camera and the PIV measurement is of course only 2D-2C (C means component of velocity). After the development of the photographical PIV, recording is digitized by means of a scanner and the output of the digital sensor is transferred to the memory of a computer directly, and such PIV system is the conventional 2D digital PIV, which is introduced in last section. The development of PIV techniques during the past 20 years has brought about a variety of PIV system. In this section, the up-to-date various types of PIV are summarized from the viewpoint of the hardware components of the system, from 2D-2C to 3D-3C PIV, and to time-resolved dynamic PIV, etc., for measurement of both macro and micro-scaled velocity field.

3.1 2D-2C PIV techniques

3.1.1 Macro scale

A typical 2D-2C PIV system is shown in Figure 1, composing with two pulsed lasers, optical lenses for laser-sheet formation, a CCD camera, a computer with PIV software installed, a timing circuit communicating with the camera and computer, and generating pulses to control the double-pulsed laser. Detailed information for the conventional macro-scaled 2D-2C PIV have been introduced in Section 2.

3.1.2 Micro scale

The fundamental difference between 2D-2C micro-scaled PIV (μ-PIV) and traditional PIV lies in the method of particle illumination (Bourdon et al., 2004a, b; Santiago et al., 1998). In traditional PIV, a thin region of the flow field is illuminated by a laser sheet, and the measurement depth is determined by the laser sheet thickness and intensity distribution. Instead of illuminating particles with a laser sheet, the entire volume of the microfluidic device of interest is illuminated, and the measurement volume depth is defined by such factors as the optics of the imaging system, wave length of emitted light, particle size (Meinhart et al., 2000; Olsen and Adrian, 2000a), the magnitude of Brownian motion (Olsen and Adrian, 2000b), and the out-of-plane velocity component (Bourdon et al., 2004a, b; Olsen and Bourdon, 2003). Figure 4 shows a typical 2D-2C μ-PIV setup, assembled about an inverted microscope system. The microfluidic device to be investigated is placed above the objective of an epifluorescent-inverted microscope. Light from the light source (mercury lamp as shown in Figure 4 or an Nd:YAG laser) enters the microscope through an aperture and is focused onto a small region of the

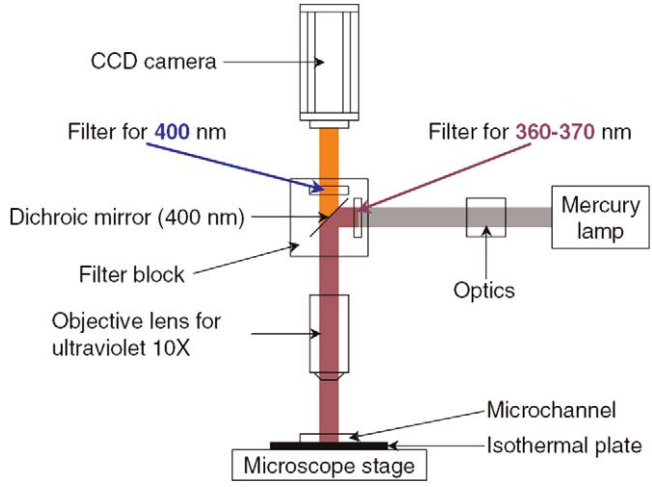

Figure 4 Schematic diagram of a typical μ-PIV (Sato et al., 2003). The light source can be mercury lamp or double-pulsed ND:YAG laser (see Plate 5 in Color Plate Section at the end of this book).

microfluidic device by the imaging objective, illuminating the entire depth of the fluid. The flow within the microfluidic device is seeded with small, fluorescent particles (order of 1 micron in diameter in general) that absorb the illuminating light and emit light at a different (usually longer) wavelength. The emitted light from the particles, as well as scattered and reflected light from light source, is long-pass filtered and imaged by a CCD camera. These filtered images containing only the light emitted by the fluorescent particles are then analyzed using PIV techniques (as described in Section 2.3) to yield the velocity vectors data. Since the camera-sampled images consist not only of in-focus particle images due to particles located at the object plane, but also out-of-focus particle images of various dimensions and intensities due to particles located away from the focal plane. Discussions on the issues associated with this major difficulty, the so-called "depth of correlation" (Olsen and Adrian, 2000a), have been well documented (Meinhart et al., 2000; Olsen and Adrian, 2000a, b). To overcome the abovementioned "depth of correlation" problem of μ-PIV, two techniques are developed, that is, selective seeding for μ-PIV and confocal μ-PIV technique.

Mielnik and Saetran (2006) designed the selective seeding technique for μ-PIV. The principles of this technique are based on selectively seeding a thin sheet of liquid within the flow in a microfluidic device. To do this, a three-layer-flow structure is generated in a microfluidic device to be investigated, by setting three inlet ports for the flow passage. Only the sheathed flow (in the center of the three) is seeded with fluorescent particles. By changing the flow rate of the other two flow streams

(without seeding and keeping the same flow rate for each), the thickness of the seeded sheathed flow can be controlled. In this manner, the measurement plane is completely defined by the particle sheet, and in principle, a measurement depth corresponding to the diameter of the tracer particles may be achieved (Mielnik and Saetran, 2006). This technique is only applicable to the flow with inherent laminar flow characteristics.

Confocal μ-PIV technique is more advanced (but expensive), and emerges after the considerable progress in the development of confocal microscopy and the advantages of this technique over conventional microscopy. This method combines the conventional PIV system with a spinning disc confocal microscope (Kinoshita et al., 2007; Lima et al., 2006, 2007, 2008; Park and Kihm, 2006; Park et al., 2004). By combining its outstanding spatial filtering technique with a multipoint illumination system, the confocal microscope has the ability to obtain in-focus images with optical thickness less than 1 μm, which is extremely difficult to achieve using conventional microscopy (Lima et al., 2006). It is therefore possible to achieve a confocal μ-PIV system with an extremely high spatial resolution, that is, true depth-wise resolved μ-PIV vector field mapping (Park et al., 2004).

3.2 2D-3C PIV techniques

2D-3C PIV techniques generally refer to the stereoscopic PIVs, which allows for the measurement of three-component velocity vectors in a 2D illuminated plane by utilizing simultaneous viewing with two cameras from two directions to obtain depth-perception. Such twin camera systems mimic the binocular vision that enables human beings to distinguish between objects near and far (Prasad, 2000). In addition to the availability to measure the third velocity component in the direction perpendicular to the laser sheet, stereoscopic PIV also adds the advantage of eliminating perspective error which exists in conventional 2D-2C PIV in the presence of out-of-plane component of velocity (e.g., Gaydon et al., 1997).

3.2.1 Macro scale

There are two basic stereoscopic configurations for the macro-scaled stereoscopic PIV: the translational method and the angular method. In the translation method, the optical axes of the camera lenses are parallel, so the image magnification is constant. A disadvantage is that the stereoscopic viewing angle must remain small (less than 30°) to avoid image distortion. The angular method can be used with much larger stereoscopic viewing angles up to the maximum of 90°. Thus, it can achieve a higher precision, and is generally preferred over the translation

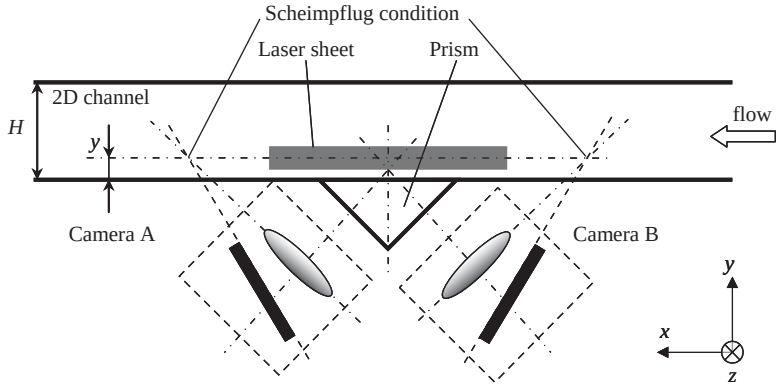

Figure 5 Schematic diagram of optical configurations for stereoscopic PIV measurement (measurement of velocity field in a *x*–*z* plane in a 2D channel flow), viewing for stereoscopic imaging with the Scheimpflug condition (Li et al., 2006a).

method (e.g., Coudert and Schon, 2001). Figure 5 shows an example of the schematic diagram of a stereoscopic PIV system with angular method.

For a stereoscopic PIV system with angular method, the image plane has to be tilted with respect to the optical axis to match the so-called Scheimpflug condition, that is, the image plane, lens plane, and object plane for each of the cameras intersect in a common line (Hinsch, 1995; Prasad and Jensen, 1995). Thus, the image magnification is no longer constant, that is, the images have a perspective distortion, and so a careful calibration procedure is necessary before any stereoscopic PIV measurement. The calibration procedure will output a space and calibration coefficient map across the image where the calibration coefficients are related to the spatial distortion of the image (Lawson and Wu, 1997). This calibration coefficient map bridges the back-projection of the data from image plane to the object plane for the reconstruction of the three velocity components. For details of stereoscopic PIV system one can refer to Soloff et al. (1997), Lawson and Wu (1997), and Prasad (2000), Raffel et al. (2007).

The calibration is a key issue before stereoscopic PIV measurement. Almost all calibrations for the reported stereoscopic PIV study utilize a target, which consists of a discrete number of markers placed on a regular Cartesian grid. However, not all the flow environment to be investigated is convenient to place a calibration target in the measurement region. To overcome this difficulty, three novel calibration methods for stereoscopic PIV are reported recently. Akedo et al. (2005) carried out a stereoscopic PIV study on flow characteristics in a cerebral aneurysm model. Since the flow passage geometry is quite irregular and it is

impossible to place and move a target plate for calibration purpose. In that reason, Akedo et al. (2005) proposed a new calibration technique using lasers. The positions of calibration points are indicated as cross-points of horizontal and perpendicular laser beams from the precisely positioned optical axis. After recording the positions of those cross-points of laser beams (each cross-point is actually reconstructed after recording two perpendicular laser beams crossing that point) by two cameras (with angular method), the calibration procedure can be performed as usual. Wieneke (2005) designed a stereoscopic PIV technique using self-calibration on particle images. This stereoscopic PIV calibration procedure is developed based on fitting a camera pinhole model to the two cameras using single or multiple views of a 3D calibration plate. The key feature of this technique is that it is possible to derive accurate mapping functions even if the calibration plate is quite far away from the light sheet, making the calibration procedure much easier. Hence, this method allows stereoscopic PIV measurements to be taken inside closed measurement volumes (Wieneke, 2005). Fouras et al. (2007, 2008) developed a novel, accurate, and simple calibration-target-free stereoscopic PIV technique utilizing three cameras. The key feature of this technique is that there is no need of a separate calibration phase but utilizes a third camera placed in paraxial (normal to the laser light sheet) position. This calibration-target-free technique offers the advantages of the calibration-target-based stereoscopic PIV, with even greater improvements in reconstruction accuracy and without the requirement of the practitioner to conduct a distinct calibration phase, and is greatest utility when the paraxial view has minimal distortion or when it is not convenient to place a calibration target in the measurement region (Fouras et al., 2007, 2008).

There are also other types of stereoscopic PIV configurations. Gaydon et al. (1997) proposed a hybrid stereo-camera combining features of translational and angular systems. Essentially, this hybrid system uses a small translation between the camera axes as well as a small inward rotation of the axes, which is for increasing the off-axis angle beyond that in an equivalent translation method, but without increasing the nonuniformity in magnification to the level of an equivalent angular method. Grant et al. (1995) introduced an in-line stereoscopic PIV system, in which the two cameras are in-line arranged and both perpendicular to the object plane. The in-line arrangement is facilitated with the use of a semi-silvered mirror placed along the common optical axis. The requirement for differing views is satisfied by using differing magnifications and object-distances for each camera. One advantage of this in-line stereoscopic system is that each particle forms images at the same angular location on each film, which makes the particle matching easier for their particle-tracking algorithm. Arroyo and Greated (1991) devised

a setup to take two stereoscopic images of the flow to be investigated simultaneously with only one camera, by means of a mirrors system. The idea is to take into account that correlating two photographs taken by two cameras can be a source of error and time consuming. Using such system, the correlation between the two photographs taken by only one camera is very straightforward and can be done automatically once everything is set up (Arroyo and Greated, 1991).

3.2.2 Micro scale

The stereoscopic μ-PIV is another version of 2D-3C PIV technique, which is based on several common components and procedures (Lindken et al., 2006) including the 2D-2Cμ-PIV method as first introduced by Santiago et al. (1998), the stereo-PIV method (e.g., Prasad, 2000), and stereomicroscopy. Figure 6 shows the schematic diagram of a stereoscopic μ-PIV system. The calibration procedure named "self-calibration on particle images" (Wieneke, 2005) has to be applied for the stereoscopic μ-PIV due to the very small confinement of the measurement target. Although preliminary results have been published from stereoscopic μ-PIV systems (Bown et al., 2006; Lindken et al., 2006), there are several limitations to this technique. A limitation is that stereoscopic μ-PIV requires a stereo-objective that typically has a low numerical aperture (NA = 0.14–0.28) and large depth-of-focus as opposed to high NA lenses (up to 0.95 without immersion) for standard μ-PIV (Lindken et al., 2006). It is also found that the accuracy of the correlation-based PIV technique is limited by the degree of overlap of the two focal planes in the stereomicroscope (Bown et al., 2006).

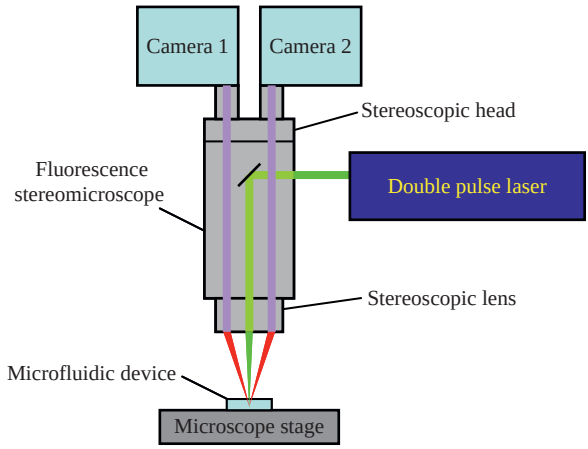

Figure 6 Schematic diagram of a stereoscopic μ-PIV system.

3.3 3D-3C PIV techniques

3.3.1 Macro scale

There have been several different 3D-3C (or volumetric) PIV techniques for macro-scaled flow measurement. Among them, holographic PIV (HPIV), defocusing PIV (DPIV), and tomographic PIV (TPIV) are the three that inherently measure all the three components of velocity field in a 3D volume. Other PIV techniques available to obtain a 3D velocity field, such as scanning PIV, dynamic PIV, that are based on some indirect algorithms to reconstruct a 3D velocity field, will be mentioned in the later sections.

3.3.1.1 Holographic particle image velocimetry. HPIV technique utilizes the interference pattern of a reference light beam with light scattered by a particle, which is recorded on a hologram, to determine the particle location in depth (Hinsch, 1995, 2002; Meng et al., 2004; Royer, 1997; Svizher and Cohen, 2006a, b), and then calculates the instantaneous 3D velocities of those particles in the illuminated volume by finding the 3D displacements of the particles between two exposures separated by a short time delay. Figure 7 depicts the principle of HPIV (Meng et al., 2004). The early HPIV systems are based on film recording of the images and so limited to double-exposure single-frame measurement. Digital HPIV emerges from about the beginning of the 21st century, which directly records a time series of holograms using a CCD camera and reconstructs the 3D velocity field through correlation-based analysis of the digital images. The evaluation method (correlation method) of the digitized data of HPIV is similar to those used in the classical 2D PIV. Although the wide application of film-based HPIV technique has been hampered by its formidable cost and technical complexity involved, the digital HPIV, with the relatively simple hardware components and the

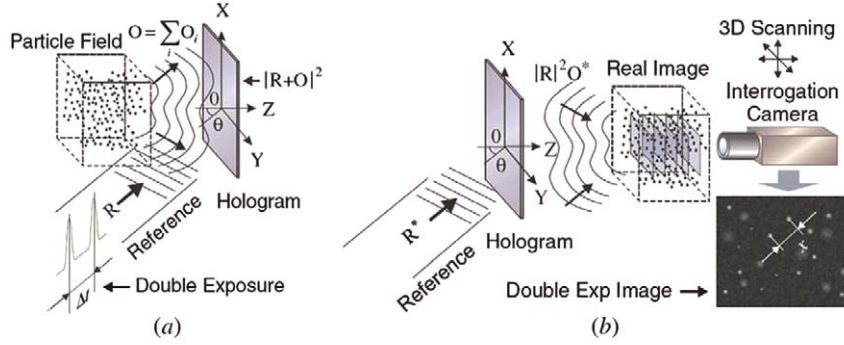

Figure 7 Principle of HPIV with traditional setup: (a) holographic recording of particle ensembles and (b) holographic reconstruction of particle images and their interrogation (Meng et al., 2004).

relative ease of operation, is hopefully to be developed and expanded as a robust, reliable, and commercialized four-dimensional (3D in space and 1D in time) flow field measurement technique.

HPIV configurations can be broadly categorized into two types based on the nature of the holographic scheme: in-line HPIV, where only one beam is employed to produce both the object wave and the reference wave, and off-axis HPIV, where separate object beam and reference beam(s) are introduced (Pu and Meng, 2000). For off-axis HPIV measurement, the seeding particles in the measured flow are illuminated with a properly expanded laser light wave, and the scattered light field from particles is stored by superposing a reference wave from the same laser source and having an oblique angle relative to the object light and recording the interference pattern on a file or a CCD sensor. The off-axis HPIV inherently requires good coherence and relies on an accurate reproduction of the reference wave for reconstruction of the image of an object, and is also easy to be suffered from vibrational noise. The in-line HPIV can provide better stability but has relatively simple arrangement and requires lower laser coherence and energy. The conventional in-line HPIV usually encounters with difficulty when the seeding particles have large density (e.g., at a level for a normal PIV measurement), since excessive speckle noise stemming from the superposition of the real image, virtual image, and reference waves may be produced to interfere with the reproduction of particle images. Another problem with in-line HPIV associated with the measurement accuracy is the large depth-of-focus in the reconstruction of particle images. Among the approaches proposed for the abovementioned problems, the in-line recording off-axis viewing technique is proved to be an efficient method to suppress the noise and improve the accuracy.

HPIV is rather complicated (and expensive) compared to 2D PIV, since it uses coherent optics for imaging, and it records, transmits, and processes information in not just two but three dimensions (Meng et al., 2004). The key issues of HPIV system are reduction of speckle noise, handling of huge quantities of data, extraction of 3D velocity in presence of large gradients and fluctuations and system complexity (Pu and Meng, 2000). Studies toward improvement of data analysis techniques for HPIV are still under development (e.g., Ooms et al., 2006, 2008). A ''universal'' HPIV scheme, that can provide successful measurements for any given flow, has not yet been proposed, and so the HPIV system requirements imposed by the flow phenomenon to be studied have to be first estimated before choosing a suitable approach (Svizher and Cohen, 2006a, b). Nevertheless, the HPIV technique has been successfully applied to measure a variety of flow phenomena, for example, 3D characteristics and statistics of a turbulent water flow in a square channel (Tao et al., 2000, 2002; van der Bos et al., 2002; Zhang et al., 1997); a cylinder wake

flow in air and a free air nozzle flow (Herrmann et al., 2000); acoustically excited air jet and the wake of a surface-mounted tab in water channel flow (Pu and Meng, 2000); large wind-tunnel flow (Herrmann and Hinsch, 2004); instantaneous topology and 3D structures of hairpin vortices in a turbulent air channel flow (Svizher and Cohen, 2006a, b); instantaneous flow fields within a motored Diesel engine (Coupland et al., 2006), and has shown its great powerfulness.

3.3.1.2 Defocusing particle image velocimetry. DPIV technique utilizes a defocusing or blurring concept to obtain information regarding a particle's position in space, as shown in Figure 8 (Kajitani and Dabiri, 2005). This concept is applied to 3D particle tracking in a flow of a vortex ring by Willert and Gharib (1992), in which a single camera with a

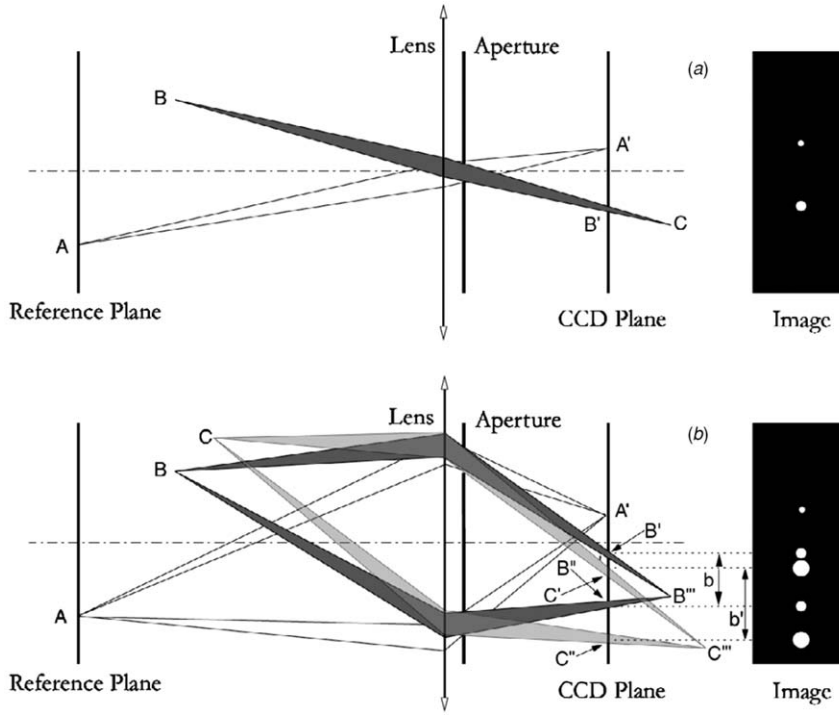

Figure 8 Defocusing concepts: (a) a standard defocusing setup with aperture on-axis; (b) defocusing setup with two off-axis apertures. Point A focuses from the reference plane onto the CCD plane; point B focuses behind the CCD plane at point B‴, leaving two slightly blurred images on the CCD plane (B′ and B′) at a distance *b* apart; point C focuses further behind the CCD plane at point C‴, leaving two slightly larger blurred images on the CCD plane (C′ and C″) at a larger distance *b*′ apart (Kajitani and Dabiri, 2005).

modified three-hole aperture is used. Lately, three individual cameras are used instead of a single one to improve accuracy with large three-hole separation (Kajitani and Dabiri, 2005; Pereira and Gharib, 2002; Pereira et al., 2000), which combines the three camera images into one image for processing to obtain the triangle-image of each particle. Pereira and Gharib (2002) introduced a DPIV system and its geometric analysis, and derive fundamental equations to estimate 3D particle locations in the measured flow field. Kajitani and Dabiri (2005) described full 3D derivations and modified equations for a DPIV system. The processing of the DPIV technique using three cameras generally includes the detection of all particle images, 2D Gaussian functions fit of the particles, identification of triplets of detected particle images forming equilateral triangles, and a 3D cross-correlation displacement estimation. The DPIV technique has been used to map the bubbly flow field in a two-blade model boat propeller (Pereira et al., 2000) and in the wake of a hydrofoil (Jeon et al., 2003), and may potentially be used to study transient flow phenomena and time-averaged statistical behavior due to its ability to acquire sequences of particle images (Kajitani and Dabiri, 2005).

3.3.1.3 Tomographic particle image velocimetry. In TPIV (as shown in Figure 9 for the principle), the pulsed light source illuminating fluid volume is viewed and recorded simultaneously from several directions by at least three digital cameras (Elsinga et al., 2006a). The setting of digital cameras is similar to stereoscopic PIV, that is, Scheimpflug condition between the image plane, lens plane, and the mid-object plane is satisfied, and so the recorded images are distorted, which requires a calibration procedure common to stereoscopic PIV to establish the relation between image coordinates and the physical space (Elsinga et al., 2006a). The cameras record 2D image projections of the 3D particle distribution in the viewed fluid volume. The 3D particle distribution is then recovered as a 3D light intensity distribution from its 2D projections, which does not rely on particle identification techniques as performed in photogrammetric PTV scheme (e.g., Maas et al., 1993). The reconstruction is an inverse problem and its solution is not straightforward: a single set of projections can result from many different 3D objects. Thus, recovering the most likely 3D distribution of particles is the topic of tomography. After reconstruction of the 3D distribution, the particle displacement (and in consequence velocity) within an interrogation volume is then obtained by the 3D cross-correlation at the two exposures, which can be an extension of any matured 2D cross-correlation algorithm to 3D. TPIV is of great attractiveness because the optical configuration is similar to a stereoscopic PIV system. The differences are only the number of cameras used and novel software for data processing. Elsinga et al. (2006a, b)

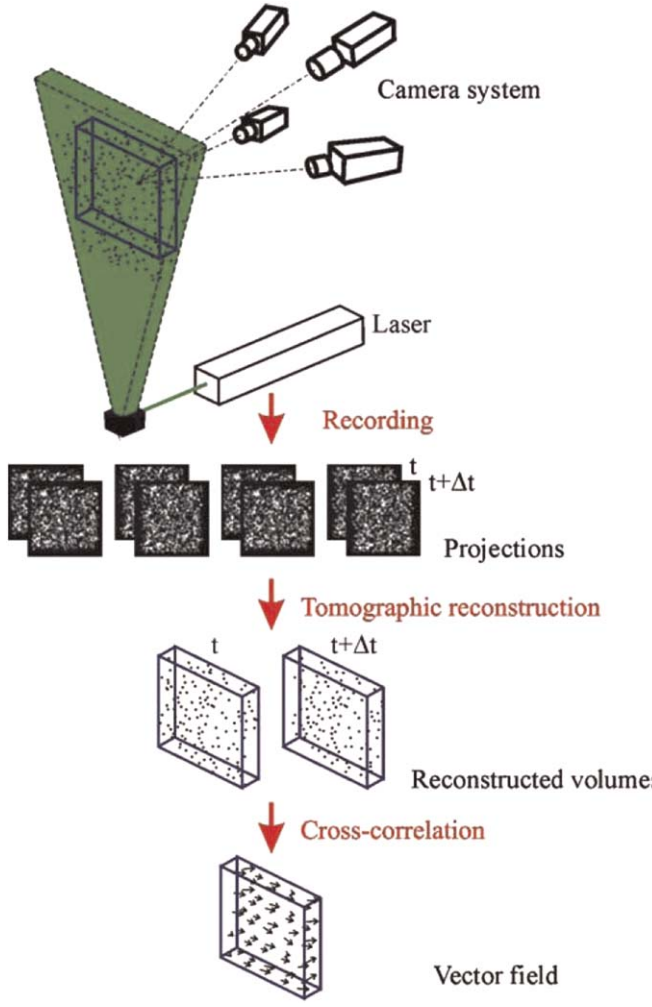

Figure 9 Principle of tomographic PIV (Elsinga et al., 2006a).

validated the TPIV technique through measurement of a circular cylinder wake flow. The results show a good agreement of the returned flow statistics compared with a stereoscopic PIV measurement (Elsinga et al., 2006b). In another feasibility study, the TPIV technique is used by Schroder et al. (2008) to time-resolved PIV recordings for the study of the growth of a turbulent spot in a laminar flat plate boundary layer and to visualize the topology of coherent flow structures within a tripped turbulent boundary layer flow. The complete time-dependent 3D velocity gradient tensor (VGT) within the measurement volume, a model of the connection of the turbulence producing Qudrant-2 and Qudrant-4 events

in a spatio-temporal flow topology, and some important aspects of Lagrangian fluid dynamics of the turbulent flow, have been successfully derived from this TPIV study (Schroder et al., 2008).

3.3.2 Micro scale

For micro scale flow measurements, there are very few papers mentioning inherent 3D-3C PIV techniques. Yang et al. (2004) introduced a digital μ-HPIV method using holographic principles, which is similar to the macro-scale HPIV technique in principle. However, holographic-based approaches need complicated system and involve difficulties with analysis and noise (Yang et al., 2004; Yoon and Kim, 2006). The μ-HPIV technique is still under development. Very recently, contrast enhancing techniques in digital holographic microscopy are discussed by Lobera and Coupland (2008). The implementation of contrast enhancing techniques as a post-processing tool increases the analysis' possibilities. Development in holographic microscopy is bound to enhance the improvement in μ-HPIV technique.

μ-DPIV is another PIV technique that inherently obtains a 3D-3C velocity field at micro scale, which goes a little further than μ-HPIV technique. Yoon and Kim (2006) and Pereira et al. (2007) described a μ-DPIV system for detecting 3D particle positions and conducting 3D velocity field measurement at micro scale via a three-pinhole defocusing concept. The basic concept of defocusing at micro scale is the same as at macro scale. In the reported μ-DPIV systems (Pereira et al., 2007; Yoon and Kim, 2006), a mask with three pinholes arranged at the vertices of an equilateral triangle is positioned on an objective lens of a microscope. The light from a seeded particle in the illuminated flow passes through each pinhole and then reaches three different positions on the image plane. The distance between the triangle vertices of the images increases with depth-wise distance between the particle position and the focusing plane, from which the particle positions in the depth direction (hence the depth-wise velocity component) can be estimated from the dimension of the triangular pattern by the defocusing concept. This μ-DPIV technique is validated through measuring the 3D flow field in a 50-μm deep micro backward-facing step (Yoon and Kim, 2006) and tracking the seeded fluorescent particles inside an evaporating water droplet at micro scale (Pereira et al., 2007). For the μ-DPIV technique, calibration procedure before the measurement is necessary (Pereira et al., 2007; Yoon and Kim, 2006).

There are also some other techniques available to obtain a 3D-3C velocity field in a micro-scaled flow passage in an indirect way, for example, using the continuity equation for a laminar flow (Bown et al., 2007; Kinoshita et al., 2007), high-speed scanning μ-PIV system using a rotating disc (Angele et al., 2006) as briefed in the later section, and so on.

3.4 Others

Apart from the abovementioned PIV techniques, there are still some other PIV systems designed for the particular purposes. Among them, the time-resolved or dynamic PIV, high-speed scanning PIV, dual-plane PIV, and simultaneous orthogonal-plane PIV are briefly introduced as follows.

3.4.1 Dynamic PIV

For a turbulent or transient flow, resolved temporal details of the flow characteristics are usually as important as the spatial structures. The appearance of kilohertz frame rate PIV, named time-resolved or dynamic PIV, allows the experimentalists to obtain the temporal and spatial information of the measured flow simultaneously. The particular parts of a dynamic PIV system different from a conventional 2D PIV includes an illumination system, which can be either pulsed lasers with a high repetition rate ranging from several to several tens kHz or a CW laser, an imaging system, which is usually a high-speed CMOS camera (or two CMOS cameras for a time-resolved stereoscopic PIV) and an accurate timing circuit (e.g., Bi et al., 2003; Burgmann et al., 2008; Li et al., 2007; Shinohara et al., 2004; Triep et al., 2005). At micro scale, a mercury lamp assembled to an epi-fluorescent microscope can also be used as light source for a time-resolved μ-PIV (Sugii et al., 2005). Other aspects other than the issues associated with the temporal resolution of the dynamic PIV, such as calibration procedures, data analysis algorithms, etc., are the same as those of a conventional 2D-2C PIV or a normal stereoscopic PIV.

3.4.2 Scanning PIV

A high-speed scanning stereoscopic PIV system is developed by Hori and Sakakibara (2004). This scanning PIV system is composed of a high-repetition-rate pulsed Nd:YLF laser, an optical scanner, and two high-speed CMOS cameras. The optical arrangement is schematically plotted in Figure 10 (Hori and Sakakibara, 2004). The laser sheet produced by the high-repetition-rate laser is scanned by an optical scanner in the direction normal to the sheet, forming an illuminated volume by collecting all the scanned laser sheets at all instants. The two CMOS cameras capture the illuminated particle images, and the stereoscopic PIV approach is adopted to construct the 3D-3C velocity distribution in the measured flow. This scanning stereoscopic PIV technique is validated with measurement of 3D vorticity field in a round water jet flow. Another type of scanning PIV technique is developed by Brucker (1997). Other than a high-speed CMOS camera for imaging at high frequency, the scanning illumination system consists of ten adjustable laser diodes in continuous mode, which can be adjusted and positioned independently,

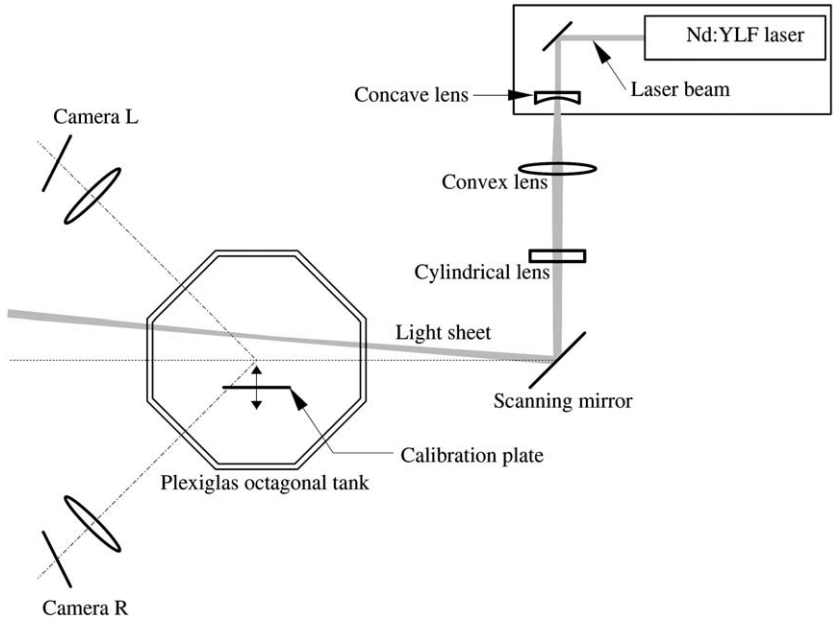

Figure 10 Optical arrangement for a high-speed scanning stereoscopic PIV (Hori and Sakakibara, 2004).

and a special electronic control allowed to pulse the laser diodes in any desired sequence or simultaneously. In this way, it is possible to form an illuminated 3D volume. This scanning PIV technique has been successfully applied to measure a laminar bubble and a transitional separation bubble on an airfoil (Burgmann et al., 2006, 2008).

At micro scale, two types of scanning μ-PIV techniques are worthy to be mentioned: a 3D scanning μ-PIV system using a piezo actuator and a high-speed scanning μ-PIV system using a rotating disc. Shinohara et al. (2005) reported the 3D scanning μ-PIV technique combining a high-speed camera, an epifluorescent microscope, a CW laser, and a piezo actuator. The piezo actuator is the unique part of this system, which is for moving the objective lens in the depthwise direction of the microscope. By inputting a current signal from a function generator, the piezo actuator equipped on the objective lens can be displaced in the depthwise direction, and so the objective lens is also moved and the information on the vertical axis (and thus a 3D velocity field) can be obtained. Angele et al. (2006) developed the high-speed scanning μ-PIV system, where the focal plane of the microscope is moved rapidly in the depthwise direction by changing the optical length using a rotating disc having glass windows with different thickness. By means of this scanning μ-PIV system, time-resolved (up to 100 Hz), pseudo-3D flow field information can be achieved.

3.4.3 Dual-plane PIV

Until now, basically two types of dual-plane PIV techniques emerged in the literature: polarization-based technique (Ganapathisubramani et al., 2005a, 2006b; Hu et al., 2001, 2002; Kahler, 2004; Kahler and Kompenhans, 1999, 2000; Liberzon et al., 2003) and frequency-based technique (Mullin and Dahm, 2005, 2006a, b). Kahler and Kompenhans (1999) first reported a dual-plane stereoscopic PIV measurement, in which two separate stereoscopic PIV systems are used to provide 3C velocity distribution in two parallel laser light sheets. This dual-plane PIV technique uses a polarization-based approach, where the two laser light sheets are arranged with orthogonal polarizations so that each stereoscopic camera pair records the scattered light from only one of the sheets. The realization of separation of the scattered light from two illuminating laser sheets with orthogonal polarization direction is based on the polarization conservation characteristic of Mie scattering, that is, in the Mie scattering regime, the scattering has a dominant forward direction and nonuniform lobed scattering towards the side directions. The polarization-based dual-plane stereoscopic PIV system consists of a four-pulse laser system delivering orthogonally polarized light, two pairs of CCD cameras set in a regular way for normal stereoscopic PIV, two high-reflectivity mirrors, and a pair of polarizing beam-splitter cubes (Kahler and Kompenhans, 2000). This technique has been successfully applied to measure all the nine components of velocity gradients in different turbulent flow fields to be investigated (Ganapathisubramani et al., 2005a, 2006b; Hu et al., 2001, 2002; Kahler, 2004).

Mullin and Dahm (2005) pointed out several drawbacks of the polarization-based dual-plane PIV technique: first, the reported experimental studies using polarization-based dual-plane PIV only measure large-scale features of turbulent flows, whereas the velocity gradients on the quasi-universal intermediate and small scales are not resolved, indicating the coarse spatial resolution of the measurement; maintaining the orthogonal polarization in the Mie scattered light requires the scattering particles to be spherical, resulting in a sever limitation to the seeding particles (fine liquid droplets are used for gas flow) and the flow environments to be investigated (only nonreacting flow is suitable to be measured). To overcome the abovementioned drawbacks, a frequency-based dual-plane stereoscopic PIV technique is developed by Mullin and Dahm (2005). The reported frequency-based dual-plane PIV system consists of four Nd:YAG lasers, two pulsed dye lasers, four CCD cameras, and an onboard timing circuit. The technique is based on two essentially independent stereoscopic PIV systems that simultaneously provide measurements in two differentially spaced data planes, by means of two different laser frequencies in conjunction with filters to separate the light scattered from the seeded particles onto the individual

stereoscopic camera pairs. Hence, the traditional seeding particles can be used as the seed, and the measurement of any reacting flows is also permitted. Furthermore, it is shown that this technique provides for significantly higher spatial resolution than the polarization-based dual-plane PIV. Mullin and Dahm (2005) stressed that the spatial resolution achieved in their measurement is a factor of 3–4 times finer than the local viscous length scale of the turbulent flow. The powerfulness of frequency-based dual-plane stereoscopic PIV is testified in the measurements of VGT fields in turbulent shear flow (Mullin and Dahm, 2006a, 2006b).

3.4.4 Orthogonal-plane PIV

The orthogonal-plane PIV technique is recently proposed for investigating the 3D characteristics of the coherent structures in a turbulent boundary layer flow (Hambleton et al., 2006; Kim et al., 2006). The hardware components and principle of this technique are the same as polarization-based dual-plane PIV. The only difference is to set up both laser sheets mutually perpendicular to each other instead of parallel to each other in the dual-plane PIV system. This allows for measuring velocity distributions in both streamwise-spanwise and streamwise-wall-normal planes simultaneously, so that the salient features of the coherent structures in a turbulent boundary layer flow as the legs and the head of the hairpin vortices can be detected (Hambleton et al., 2006; Kim et al., 2006).

4. MEASUREMENT OF MULTIPHASE FLOW USING PARTICLE IMAGE VELOCIMETRY

Since the term ''particle image velocimetry'' being first proposed in 1984 (Adrian, 1984; Adrian, 2005; Pickering and Halliwell, 1984), the development and application of PIV techniques have been flourished in the research fields of measurement science and technology, turbulence, fluid mechanics, fluid engineering, aerodynamics, multiphase flow, combustion, granular flow, microfluidics, cryogenics, biological fluid dynamics, etc. Among the published experimental studies using PIV, one of the most successful application areas of this technique could be, for example, the detection of the coherent vortical structures and investigation of its statistical characteristics of wall-bounded turbulent flows without or with control (Adrian et al., 2000a, b; Adrian, 2007; Carlier and Stanislas, 2005; Christensen and Adrian, 2001; Ganapathisubramani et al., 2003, 2005a, b, 2006a, b; Hambleton et al., 2006; Hou et al., 2008; Hutchins et al., 2005; Kahler, 2004; Kim et al., 2006; Liu et al., 2001; Li et al., 2005a, b, 2006a, b, 2008; Longmire et al., 2003; Natrajan et al., 2007;

Svizher and Cohen, 2006a, b; Tao et al., 2000, 2002; Tomkins and Adrian, 2003; Warholic et al., 2001; White et al., 2004, among others). Experimental investigation on a multiphase flow by means of PIV technique might have some additional complexity and difficulty as compared with its single-phase counterpart. Besides that images taken by a PIV system are statistically analyzed to construct the velocity vectors, the patterns or intensity distribution of the images taken for a multiphase flow can also be used for phase-resolution, providing further information for multiphase flows in addition to the velocity field. The existence of different phases in a multiphase flow may bring about additional problems to a normal PIV measurement, such as strong reflection at the interface between two phases (particularly gas–liquid interface), problems associated with different refractive index of two phases, precisely distinguishing two phases, and so forth. Compared with PIV techniques for the single-phase flow, multiphase flow PIV measurement usually needs additional analytical algorithms or even supplementary technique(s), for example, LIF technique is often used together with PIV to resolve gas and liquid phases as well as the velocity field. Hence, some issues associated with measurement of multiphase flows using PIV technique are introduced in this section. Note here that the "multiphase" here holds extensive meaning that the multiphase flow to be investigated cannot only include different phases (states of matter) such as a gas–liquid two-phase flow, but also include same phases but different fluids such as a liquid–liquid two-fluid flow.

4.1 Liquid–liquid two-fluid flows

Although the liquid–liquid two-fluid flow has the same phase in the viewpoint of state of matter, some problems might be encountered when utilizing PIV to measure the velocity field(s) in one or both of fluid flows, such as mismatching of refractive indices of the two fluids, physical properties that influence the mixing of seeding particles, resolving the two fluids from each other, etc.

It is usually necessary to match the refractive indices of two fluids (and the transparent wall of flow passage in some cases particularly for microchannel flow). For example, in an experimental study on the self-preserving structure of steady round buoyant turbulent plums in cross flow (Diez et al., 2005), planar-LIF (PLIF) and PIV techniques are utilized to measure the mean concentration of source fluid and mean velocity fields simultaneously. Both PLIF and PIV measurements in this study necessitate matching the indices of refraction of the source (water solution of potassium phosphate, monobasic KH_2PO_4, containing Rhodamine 6G dye) and ambient fluids (ethyl alcohol/water) to avoid scattering the laser beam away from the buoyant flow. Visual inspection

of different instantaneous PLIF images taken with and without index matching does show obvious effect when the indices of the source and ambient fluids are not matched: blurred islands appear on the PLIF image without index matching (Diez et al., 2005). Resolving the source and ambient fluids from each other can be straightforwardly realized by detection of the PLIF images: color part represents the source fluid containing dye and colorless part represents the ambient fluid.

Creating staggered flow in a microchannel to generate 3D internal circulation within liquid droplets or liquid slugs is one of the hot topics in the research field of microfluidics with various application backgrounds such as creation of diverse and individually addressable sample stacks for serial processing, narrow residence time distributions, enhancement of mixing capabilities, and so on (Gunther et al., 2005; Kashid et al., 2005; Kinoshita et al., 2007; Malsch et al., 2008; Sarrazin et al., 2006). To explore the 3D flow characteristics μ-PIV techniques are widely used as well as numerical simulations. A comprehensive 3D measurement and visualization of internal flow features of a moving droplet in a polydimethylsiloxane (PDMS) microchannel are carried out by Kinoshita et al. (2007) using high-speed confocal μ-PIV technique. Water solution of glycerol is pumped into a microchannel flow of silicone oil, which is immiscible with glycerol solution, through a T-shaped branch, and torn off at the outlet of the branch by the oil-phase flow to form droplets. The most important advantage of confocal μ-PIV is the high resolution in the depthwise direction, which is realized by the fact that the light from out-of-focus particles is cut off optically and only the illuminated particles in the focal plane are imaged at high contrast. To accomplish the full advantage of confocal μ-PIV measurement, however, it needs to eliminate any negative factors including the refractive index mismatching problem. To minimize the refraction and reflection of light at the liquid–liquid and liquid–solid interfaces, the refractive indices of the working fluids (water solution of glycerol and silicon oil) and the channel material of PDMS have to be matched. The silicon oil has a refractive index of 1.414, which is only slightly different from that of PDMS 1.412. A mixture of 45% water and 55% glycerol with a refractive index of 1.414 is adopted to be the droplet liquid. By such relatively precise treatment, the 3D velocity field (with the aid of continuity equation for the out-of-plane velocity component) and hence the 3D recirculation internal flow characteristic is clarified (Kinoshita et al., 2007). Velocity distribution in the oil phase is usually difficult to measure by means of μ-PIV because of the lack of suitable seeding particles (Kinoshita et al., 2007; Malsch et al., 2008). In some other experimental studies on liquid–liquid two fluid flows in a microchannel by means of μ-PIV, however, issues about the matching of refractive indices are not mentioned (Gunther et al., 2005; Kashid et al., 2005; Malsch et al., 2008;

Sarrazin et al., 2006, among others). Note that these studies use a normal μ-PIV system instead of confocal μ-PIV. The negligence of mismatching of refractive indices might be due to the fact that the normal μ-PIV is relatively insensitive to the effect of refractive indices on the depthwise resolution compared with its confocal counterpart, and the channel wall is flat with zero curvature.

4.2 Gas–liquid two-phase flows

Among all the researches on multiphase flows in the published literature, those on gas–liquid two-phase flows holding the largest volume might be pertinent. It might also be the case for PIV measurement of multiphase flow. The PIV investigations on gas–liquid two-phase flows that simultaneously measure velocity field in one or both of the two phases and resolve the gas–liquid interface are discussed in this section. The key issue associated with such kind of PIV measurement of gas–liquid two-phase flows is how to overcome the complexity and difficulty stemming from the influence of gas–liquid interface on the illuminating and imaging of PIV. Experimental studies on gas–liquid two-phase flows using PIV techniques (in some cases supplemental techniques like LIF are needed) to both measure the velocity distribution and distinguish different phases can be largely categorized into three groups: liquid free-surface flow, bubbly flow, and gas–liquid two-phase flows in micro-channels.

4.2.1 Free-surface flow

Free-surface flow with interfacial transport processes is a subject of great interest since its effects can be seen both in nature and practical devices, such as the air–sea interface, ship wakes, and chemical processes like gas-absorption equipment. In many cases, it is necessary to investigate the interaction of the flow and the free surface or correlate the free-surface deformation with the flow characteristics beneath the liquid surface. To this end, PIV technique can be applied to some free-surface flows as a powerful experimental tool.

Li et al. (2005c) reported an approach for simultaneously measuring the turbulent velocity field and surface wave amplitude in an open-channel flow by means of a conventional PIV system only. The experimental facility is shown in Figure 11. PIV measurement is performed in the x–y plane following the coordinate system shown in Figure 11. The construction of velocity field in the illuminated liquid phase is according to the well-documented procedures as introduced in Section 2. The determination of free-surface level is based on such a fact that the gas and liquid phases are shown by different patterns on a PIV image, that is, a relatively bright region for the gas phase and a dark

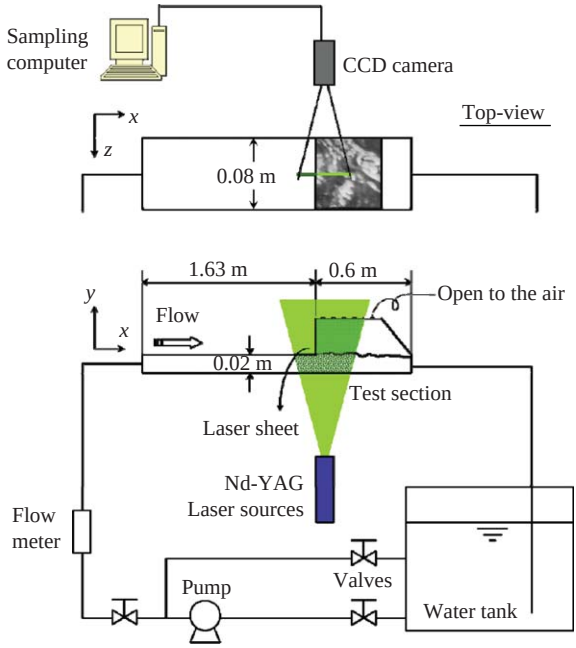

Figure 11 Schematic diagram of the experimental facility for simultaneous measurement of turbulent velocity field and free-surface wave amplitude in an open channel flow using PIV (Li et al., 2005c).

region with dense bright points (illuminated tracing particles) for the liquid phase, which allowed for the free-surface level to be automatically detected by an algorithm.

Figure 12 shows an example of a PIV image and the free-surface-level tracking procedure. First, the intensity of contrast of each pixel on a PIV image is digitized. The programmed surface-tracking algorithm (developed using the MATLAB language) is then applied to the digitized matrix of contrast intensity. Instead of inspecting the intensity of contrast at each pixel, the local standard deviation, $\tilde{p}(x_i, y_j)$, of the contrast intensity in a window of 3×3 pixels is calculated for each pixel to obtain a new matrix of $\tilde{p}(x_i, y_j)$. The value of $\tilde{p}(x_i, y_j)$ is low at the gas-phase region on a PIV image and high at the liquid-phase region. The matrix of $\tilde{p}(x_i, y_j)$ is then filtered to screen out the spikes of low $\tilde{p}(x_i, y_j)$ that would hinder the determination of the free-surface based on a threshold value of $\tilde{p}(x_i, y_j)$. This procedure was done by extracting and recording the local maximum $\tilde{p}(x_i, y_j)$ in a window of 3×3 pixels. Figure 12b shows an example of the filtered map of $\tilde{p}(x_i, y_j)$ corresponding to the rectangular area marked in Figure 12a. To determine the free-surface level, two threshold values are used, as shown in Figure 11c plotting the profile of

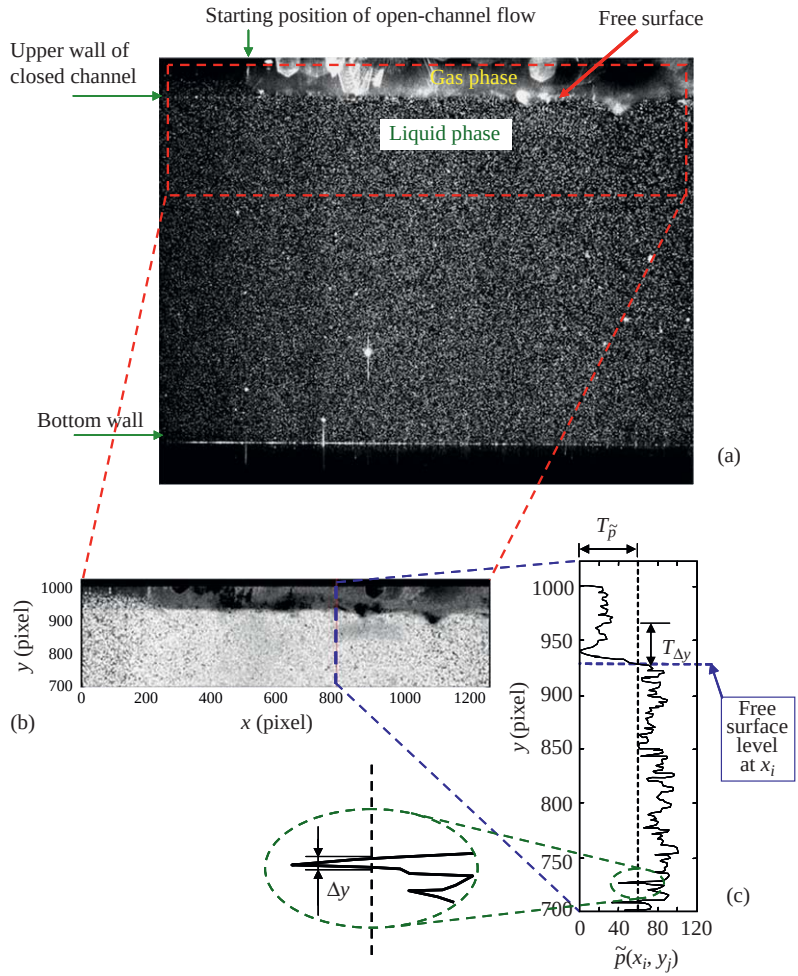

Figure 12 An example of a PIV image and the free-surface level tracking procedure: (a) PIV image showing interfaces and different phases; (b) 2D distribution of filtered local standard deviation of the contrast intensity; (c) distribution of filtered local standard deviation of the contrast intensity at $x_i = 800$ pixels showing the determination of free-surface level (Li et al., 2005c).

$\tilde{p}(x_i, y_j)$ at $x_i = 800$ pixels. The first threshold value $T_{\tilde{p}}$ was set so that $\tilde{p}(x_i, y_j)$ generally below $T_{\tilde{p}}$ at the gas-phase region and mostly above $T_{\tilde{p}}$ at the liquid-phase region. Although filtering has been applied to $\tilde{p}(x_i, y_j)$ to screen out the low-value spikes, points at which $\tilde{p}(x_i, y_j)$ is lower than $T_{\tilde{p}}$ may still remain, which calls for the second threshold value, $T_{\Delta y}$, as shown in Figure 12c. Δy is the interval in which the points have the $\tilde{p}(x_i, y_j)$ value lower than $T_{\tilde{p}}$ and out of which $\tilde{p}(x_i, y_j)$ values are larger

than $T_{\tilde{p}}$. On the basis of these two threshold values, the free-surface level at x_i satisfies the following constraints: $\tilde{p}(x_i, y_{j-1}) > T_{\tilde{p}}$ and $\tilde{p}(x_i, y_{j+k}) < T_{\tilde{p}}, k = 1, 2, \ldots, T_{\Delta y}$. The obtained profile of free-surface level at all the streamwise locations is then smoothed by using the zero-phase filter. The position of the bottom wall of the channel, upper wall of the closed channel, and the starting point of the open-channel flow can be directly determined from the PIV image, as shown in Figure 12a.

Figure 13 plots an example of the processed PIV frame. The turbulent velocity field and its boundaries, solid wall, and liquid-free surface are simultaneously shown in Figure 13. The turbulence structures such as the coherent vortical structure near the bottom wall and its modification after release from the no-slip boundary condition near the free surface of the open-channel flow, and the evolvement of the free-surface wave can be seen in Figure 13. This simultaneous measurement technique for free-surface level and velocity field of the liquid phase using PIV has been successfully applied to the investigation of wave–turbulence interaction of a low-speed plane liquid wall-jet flow (Li et al., 2005d), and the characteristics of a swirling flow of viscoelastic fluid with deformed free surface in a cylindrical container driven by the constantly rotating bottom wall (Li et al., 2006c).

Several alternative algorithms for detection of free-surface level in PIV images have also been reported in the literature. Zarruk (2005)

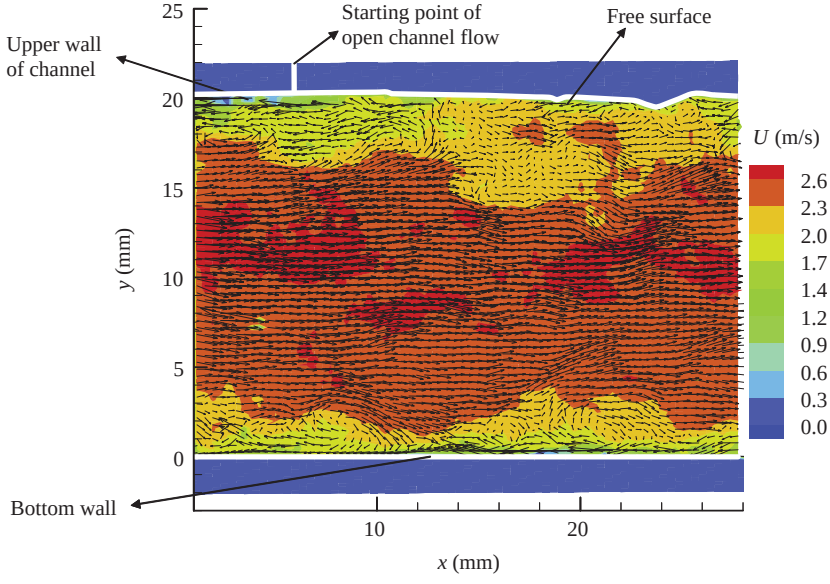

Figure 13 An example of the processed PIV frame, including turbulent velocity field and the position of the wavy free surface (Li et al., 2005c) (see Plate 6 in Color Plate Section at the end of this book).

proposed a measurement method for the free-surface deformation in PIV images, in which the gradient of the image intensity in each column, $\partial I/\partial y$, is calculated, and then the location of the maximum gradient is labeled as the potential free-surface location. If the free surface is well illuminated, it is sufficient to obtain the location of the maximum intensity gradient or the location of the maximum intensity to identify the location of the free surface (Zarruk, 2005). Misra et al. (2006) described an estimation algorithm based on gray-level co-occurrence matrix (GLCM) and ''snakes'' (parametric in conjunction with geometric active contours) to calculate the air–water interface from PIV images of an air-entraining laboratory hydraulic jump. Active contours minimizing energy functionals based on the internal (controlling the shape of the contour) and external (characterizing image information) energies of the contour are used to increase the accuracy of the predicted interface. This method is relatively complicated, but has the ability to give a first approximation to the location of the complex turbulent water-free surface. In the turbulent hydraulic jump experiment, the free air–water interface is compared to the visually interpreted interface and the deviation is found to be within the typical measurement resolution for the fluid velocities (Misra et al., 2006).

Another aspect of PIV investigation of a free-surface flow is to measure the gas side velocity over a liquid surface, in which identification of the gas–liquid interface is also necessary. Reul et al. (1999, 2008) reported the velocity measurements in the crest–trough region above the water surface using PIV technique. The dynamics of instantaneous velocity and vorticity structures in the near-surface flow are discussed in detail. Shaikh and Siddiqui (2008) reported an experimental investigation of the airflow structure in the immediate vicinity of the wind-sheared air–water interface using PIV technique. To obtain reliable estimates of the near-surface velocity, it is necessary to locate the water surface accurately. In the experiment (Shaikh and Siddiqui, 2008), the contrast between the air and water is improved by dissolving dark blue food color in the water before PIV measurement, resulting in the uniform grayscale value in the waterside regions of the PIV images. This allows for the implementation of a simple image processing technique to identify the air–water interface. In this way, both location of air–water interface and velocity distribution in the vicinity of the interface are obtained precisely (Shaikh and Siddiqui, 2008).

4.2.2 Bubbly flow

In the industry of chemical process, nuclear engineering, maritime engineering, environmental engineering, etc., there is a vast interest in the behavior of gas–liquid two-phase flows with bubbles involved. Although computational fluid dynamics (CFD) is a powerful tool that is

being used to simulate the multiphase flow behavior, there is still a lot of dispute about the formulation and closure of the fluid dynamical equations of theoretical and empirical models. This calls for the need for experimental validation of CFD. PIV technique is one of the measurement approaches and has received a lot of attention for this purpose in the past two decades.

Lindken et al. (1999) reported a PIV measurement of velocity field in multiphase flows, where a digital mask in combination with the minimum quadratic difference (MQD) method (Gui and Merzkirch, 1996) is adopted to enhance the evaluation of velocity field in the contact area between the gas and liquid phases. The application of digital mask technique is allowed by the fact that the sizes of gas bubbles and tracer particles seeded to liquid phase appearing on the PIV images have significant differences. Lindken and Merzkirch (2000) extended the combination technique of MQD-based PIV and digital mask to simultaneously measure the 3D shape, position, and velocity of the bubbles and the 2D pseudo-turbulence velocity distribution induced by the bubbles in the liquid phase. To obtain the 3D information of the bubbles, a second, independent illumination and recording system, which provides a laser light sheet perpendicular to the PIV light sheet and records the in-plane images by a high-speed camera, is used simultaneously in addition to a normal PIV system as applied by Lindken et al. (1999). From a time series of the images of the recorded bubbles taken with the additional system and the rise velocities measured by PIV, a 3D picture of the system of bubbles including an estimate of the bubbles' size and shape can be reconstructed. Hence, full information on the instantaneous 3D bubble positions and velocities, and the 2D-2C velocity field of the water flow is achieved. Hassan et al. (1998) carried out an investigation of 3D two-phase flow structure in a bubbly pipe flow using a PIV system together with other three digital cameras. In addition to the measurement of velocity field in the liquid phase, the bubble's shape is reconstructed based on the dynamic generalized Hough transform algorithm. The DPIV technique was also successfully applied to the measurement of bubbly flow (Jeon et al., 2003; Pereira and Gharib, 2002; Pereira et al., 2000), in which high resolution images of the bubble field were recorded and analyzed to provide both bubble size, bubble location, and bubble velocity field within a cubic foot volume. The velocity vectors of the bubbles were computed from the volumetric cross-correlation of consecutive 3D sets of bubble locations and the bubble size information was abstracted from the bubble-scattered peak intensity.

Although some experimental studies on multiphase flow using PIV-only technique have been reported, the presence of the dispersed gas bubbles or columns usually introduces problems to the PIV measurement. Deen et al. (2002) provided an example of PIV image taken in a

bubbly flow at a void fraction of approximately 1%. It indicates at least the following problems: in the subregion on the PIV image where the bubble concentration is rather high, there is little space left for the tracer particles, resulting in low valid detection probability; the dispersed phase can introduce shadows, which together with bubbles in front of the light plane reduce the amount of information present in the PIV images; and the deformation of gas bubbles during the time delay between the two recordings of the flow may deteriorate the precision of the PIV measurement (Deen et al., 2002). To overcome those problems emerged in PIV measurement of bubbly flow, several advanced techniques have been developed, such as DPIV technique as introduced in Section 3.3, combination of PIV with one or both of LIF technique and shadow image technique (SIT), etc. Nevertheless, PIV measurement technique used for bubbly flow is limited to relatively low volume fractions of the dispersed phase.

When merely a PIV system is used for the measurement of a bubbly flow, the intensity of light reflected from the bubbles' surface not only saturates the CCD camera but also overwhelms the intensity of light refracted from the seeding particles for PIV in its vicinity. Philip et al. (1994), Broder and Sommerfeld (2002), and Liu et al. (2005) hence used the hybrid PIV–LIF technique (wavelength discrimination), that is, fluorescent seeds and appropriate filters (LIF technique) are adopted to distinguish between the light reflected by the liquid–gas interface and the light refracted by the surrounding tracer particles, in their experimental studies on the characteristics of steam bubble collapse, a laboratory bubble at higher void fractions, or bubble-induced flow structure.

To clarify the mutual interactions between the gas bubbles and its surrounding liquid flow (mostly turbulent) in a bubbly flow, information of bubble's shape and motion is one of the key issues as well as the surrounding liquid velocity distribution. Tokuhiro et al. (1998, 1999) enhanced the PIV/LIF combination technique proposed by Philip et al. (1994) with supplementation of SIT to simultaneously measure the turbulent flow velocity distribution in liquid phase around the gas bubble(s) and the bubble's shape and motion in a downward flow in a vertical square channel. The typical experimental setup of the combination of PIV, LIF, and SIT is shown in Figure 14. The hybrid measurement system consists of two CCD cameras; one for PIV/LIF (rear camera) and the other for SIT (front). The fluorescent particles are Rhodamine-B impregnated, nominally 1–10 μm in diameter with specific density of 1.02, and illuminated in a light sheet of approximately 1 mm thickness (Tokuhiro et al., 1998, 1999). The fluorescence is recorded through a color filter (to cut reflections) by the rear camera. A shadow of the gas bubble is produced from infrared LEDs located behind the gas bubble. A square ''window'' set within the array of LEDs provides optical access for

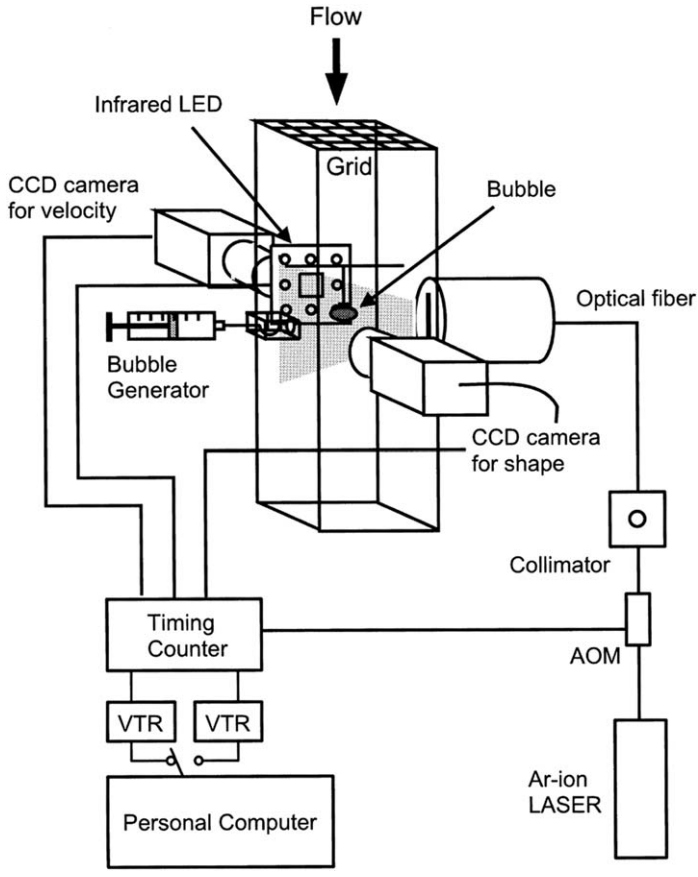

Figure 14 Schematic diagram of a hybrid PIV/LIF/SIT system used for measuring liquid-phase velocity distribution and bubble's shape and motion (Tokuhiro et al., 1998).

PIV/LIF. The emitted light is filtered through a translucent cover sheet and produces a shadow of the bubble, which is then captured by the front CCD camera. To capture the bubble's shape and the surrounding liquid flow field simultaneously, the triggering of the laser, the LEDs, and the two CCD cameras are synchronized by a timing circuit.

Figure 15 shows an example of typical images of the illuminated tracer particles for PIV/LIF and the SIT images of two bubbles in three representative positions. It is clearly seen that the tracer particles in the wake and a partial outline of the bubble boundaries are visible on the PIV image. The number of tracer particles is sufficient enough to calculate velocity vectors through the normal cross-correlation-based PIV algorithm.

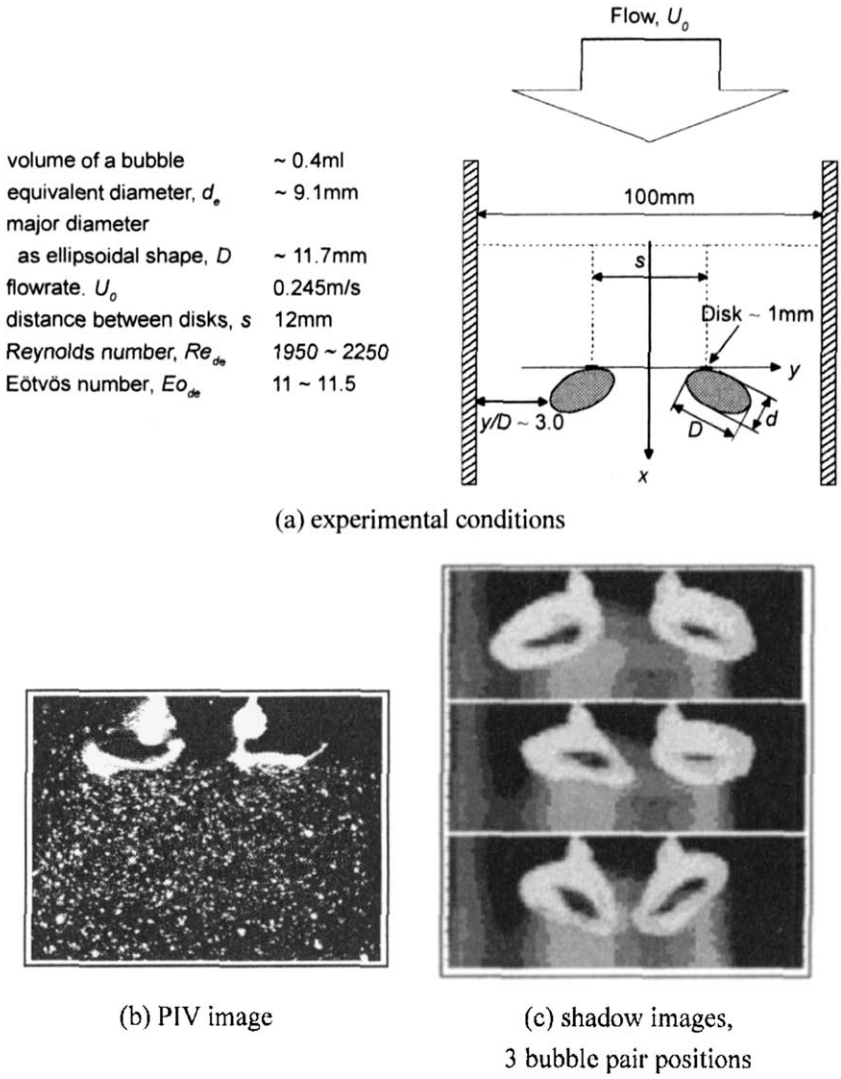

Figure 15 An example of PIV/LIF/SIT taken images: (a) schematic of experimental conditions and ranges; (b) typical PIV image showing illuminated tracer particles around the two bubbles; (c) typical shadow images of the two bubbles at three instants (Tokuhiro et al., 1999).

A representative time sequence of four PIV/LIF-derived velocity vector distributions together with the SIT-derived bubble shadows is plotted in Figure 16 as a typical result obtained by the PIV/LIF/SIT system. Note that even with LIF technique used, there are also ''white-out'' regions (intensity saturation), and the laser sheet entering from the

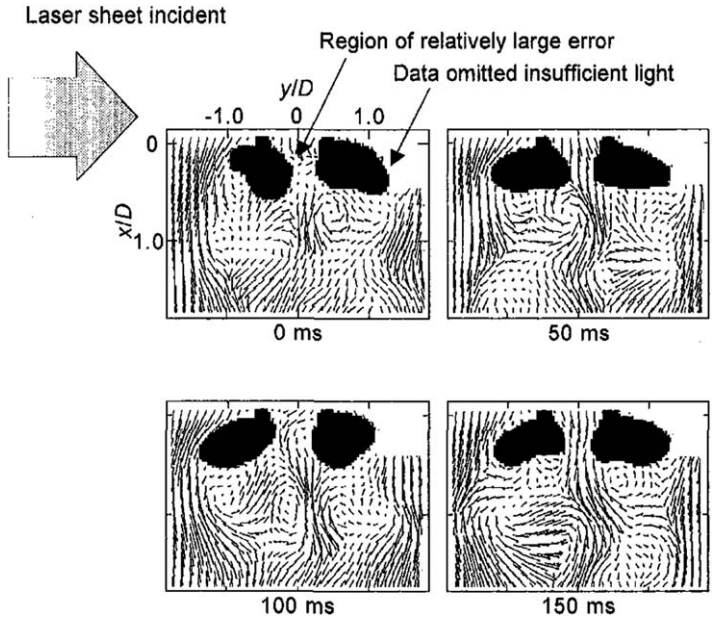

Figure 16 An example of PIV/LIF/SIT taken turbulent velocity fields in the wake region of two bubbles together with the bubble shadows at four instants (Tokuhiro et al., 1999).

left cannot illuminate the regions in between the two bubbles and to the far right, resulting in either relatively large error of or lack of velocity vectors locally, as can be seen from Figures 15b and 16. Nevertheless, the detailed behaviors of gas bubble(s) subjected to a liquid flow, the characteristics of the wake flow behind the bubble(s), the interactions between the two bubbles, and between bubble and surrounding liquid-phase flow have been explored successfully by means of the hybrid PIV/LIF/SIT technique (Tokuhiro et al., 1998, 1999).

Tokuhiro et al. (1998, 1999) applied the hybrid techniques of PIV/LIF/SIT to a relative simple bubbly flow case, that is, with one or two bubbles involved. The application of this technique to a normal bubbly flow with many bubbles but at low void fraction can be extended straightforwardly. An experimental study on the effect of bubble diameter on modification of turbulence in an upward bubbly flow in pipe is carried out by Fujiwara et al. (2004b) using the PIV/LIF/SIT system as measurement technique. Since many bubbles are involved in this bubbly flow, some additional procedures for the detection of bubble shapes and positions are provided, which include (1) obtaining the background image from the average of more than 1,000 SIT images in a time series; (2) detecting the bubble-like objects by subtracting the

background image from the original images; (3) changing the bubbles in focal plane images to be binary (black–white) by using a certain threshold level of light intensity; and (4) adopting the roundness, given by $L^2/4\pi A$, where L and A are the circumference length and area of the object, to prevent miss-recognition of overlapped bubbles as single bubbles and remove irregular images. Figure 17 gives an example of both PIV/LIF and SIT images and the final reconstruction of velocity field together with the bubble images (Fujiwara et al., 2004b).

Furthermore, Fujiwara et al. (2004a) performed an experimental study using PIV/LIF combining with double-SIT to construct approximated 3D shape deformation of bubbles as well as to investigate quantitatively the 3D wake flow structures behind bubbles in a simple shear flow. The

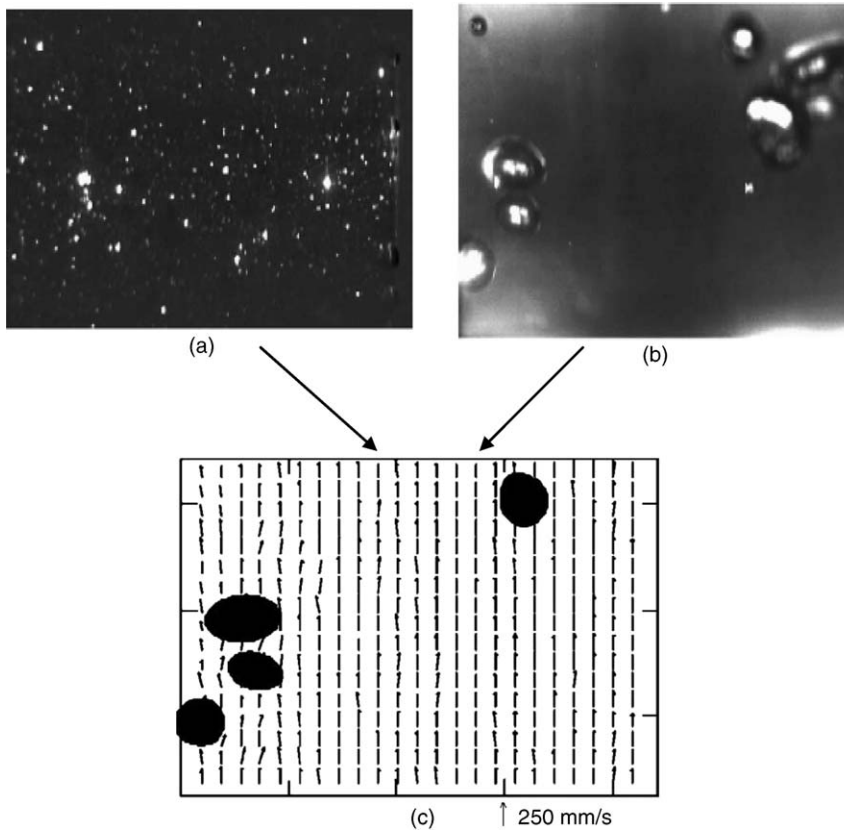

Figure 17 An example of PIV/LIF/SIT-measured velocity field together with the bubble shapes and positions in an upward bubbly flow: (a) PIV image with fluorescent tracer particles; (b) SIT snapshot with bubble shadow images at the same instant as (a); and (c) velocity vector field together with detected bubbles reconstructed from (a) and (b) (Fujiwara et al., 2004b).

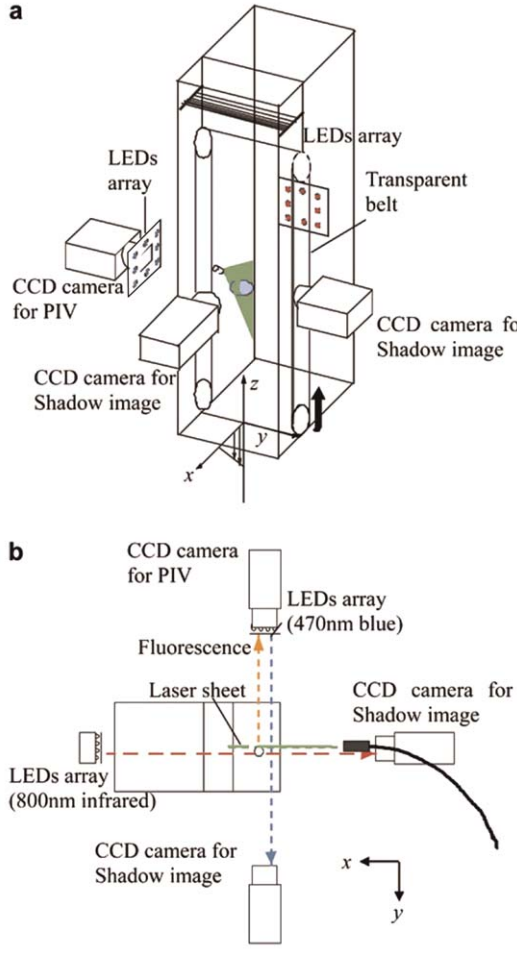

Figure 18 Schematic of experimental setup for measurement of 3D bubble deformation and flow structure in the wake using the combination of PIV/LIF and double-SIT: (a) schematic of the measurement system; and (b) top view of the experimental facility (Fujiwara et al., 2004a).

combination system of PIV/LIF and double-SIT is schematically shown in Figure 18 (Fujiwara et al., 2004a). The vertical shear flow is produced between the looped transparent belt driven by a variable-speed motor and the channel wall. The measurement system consists of three CCD cameras: one for PIV/LIF and the other two set perpendicularly to each other for detecting the bubble shape in two planes, from which the approximated 3D bubble shape can be reconstructed. A timing circuit is built for simultaneously synchronizing the triggering of the laser, the LEDs, and the three CCD cameras.

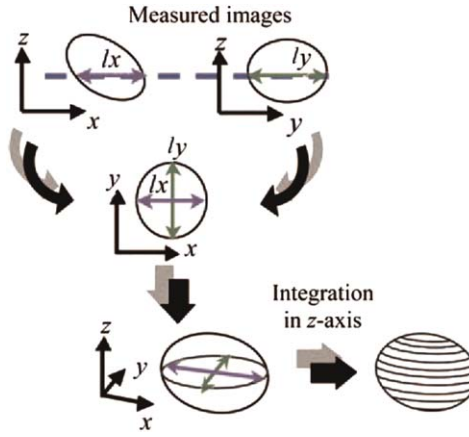

Figure 19 Approximation of 3D bubble shape from the bubble shadow images taken in two perpendicular planes (Fujiwara et al., 2004a).

The post-processing procedure is almost the same as that in PIV/LIF/SIT measurements (Fujiwara et al., 2004b; Tokuhiro et al., 1998, 1999) except for the approximation of the 3D bubble shape and tracing its trajectory. The reconstruction of 3D bubble shape from the recorded SIT images in two planes perpendicular to each other is realized by an approximation method. Figure 19 depicts the schematic of the reconstruction procedure. First, the bubble's x–y cross-section (following the coordinate provided in Figure 19) is assumed to be ellipsoid. Then, the SIT images of bubble in both the x–z and y–z planes allow the estimation of the length of the major and minor axes of the ellipsoidal x–y cross-section at each position in the z direction. Finally, the instantaneous 3D bubble shape can be reconstructed by integrating each x–y cross-section in time series. The approximated 3D bubble shape, the trajectory of the bubble in time series, and the corresponding flow structures calculated by PIV technique are plotted in Figure 20 as an example. With the full information, the detailed characteristics of the bubble transition path, the interactions between the deformed bubble, and the 3D wake flow structure, etc. have been investigated (Fujiwara et al., 2004a).

An extended version of the hybrid technique of PIV/LIF/SIT is reported by Kitagawa et al. (2005), in which the PTV technique is employed to measure the velocity field in liquid phase and track the velocity distribution of dispersed bubbles, in addition to the SIT measurement of bubbles' shape and location in a microbubble-laden turbulent channel flow. It is well known that microbubbles injected into the turbulent boundary layer developing on a solid wall have a significant skin friction reduction effect. To investigate the interactions between the injected microbubbles (the void fraction is actually low but

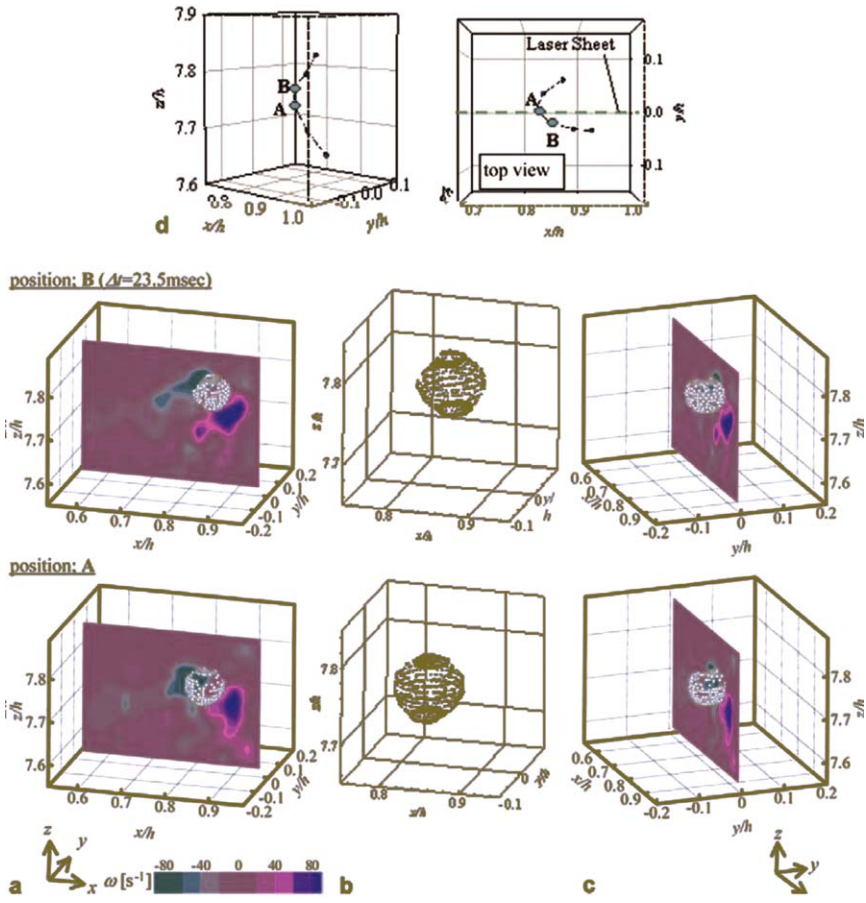

Figure 20 An example of the approximated 3D bubble shape and corresponding flow structure estimated from the measurement using PIV/LIF combining with double-SIT system: (a) characteristic vorticity structure around the bubble (bubble moves in the *y*–*z* plane); (b) reconstructed 3D bubble shape; (c) relation between bubble location and measured plane for PIV; and (d) 3D bubble trajectory (Fujiwara et al., 2004a) (see Plate 7 in Color Plate Section at the end of this book).

the number of microbubbles is huge) and turbulence structures in a turbulent channel flow of water, which is the key point of understanding the drag-reduction mechanism of microbubble-injection method, an experimental study using the combination system of PIV/LIF/SIT is thus designed by Kitagawa et al. (2005). For the measurement of liquid turbulent flow with large number of bubbles involved, the PTV technique instead of cross-correlation-based PIV algorithm is employed. This is because liquid velocity vectors in high accuracy are usually difficult to be estimated with increase of void fraction with PIV

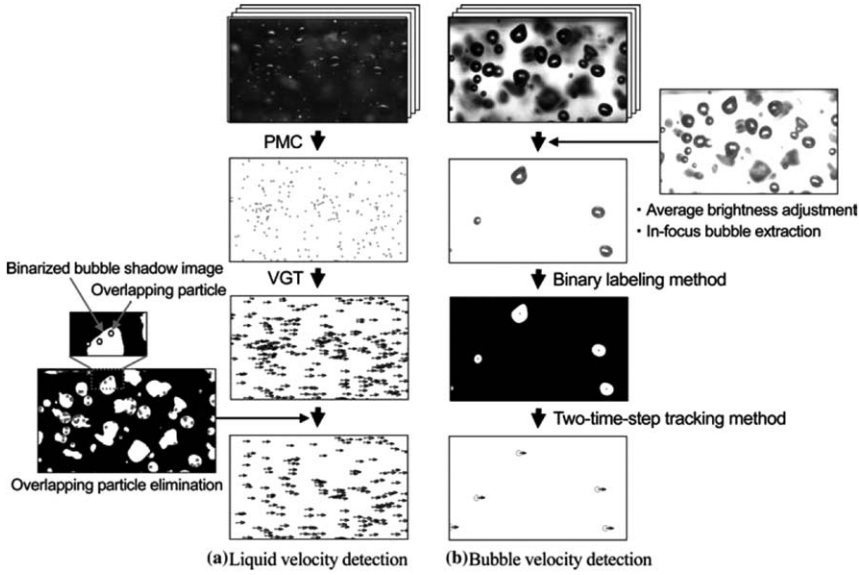

Figure 21 Flow chart of the processing procedure of PIV/LIF/SIT-taken images for liquid phase and bubble velocity estimation by means of PTV technique (Kitagawa et al., 2005).

technique, which originates from the decrease of inter-bubble gaps in relation to the interrogation window dimensions and the increase of liquid fluctuation velocities induced in the bubble wake.

The data-processing procedures of both PIV/LIF and SIT images for estimation of velocity distribution in liquid phase and of bubbles, respectively, using the PTV technique, are illustrated in Figure 21. The PTV procedures for measuring the liquid-phase velocity field are twofold: first, by using the particle mask correlation (PMC) approach (Takehara and Etoh, 1999), the centroid of each fluorescent tracer particle is calculated from the original PIV images; then, the velocity vectors of individual fluorescent tracer particles are calculated by the VGT method (Ishikawa et al., 2000) with a time interval of 26 μs between pairs of images. The procedure for measuring the bubbles' velocity vectors, without considering the in-focus overlapping bubbles, is as follows: first, the average brightness of the original SIT images is adjusted to emphasize the edges of the bubbles and to remove the noise, and then only in-focus bubbles are extracted; then, the centroids of the bubbles are estimated from the images with invert-brightness and binary treatment using the binary-labeling method (e.g., Yamamoto et al., 1996); at last, the velocity vectors of the bubbles are simply calculated from bubble positions in two frames. To accurately obtain the velocity of the liquid phase, tracer particles that overlap with the bubble SIT images are regarded as bad points and need to

be eliminated in the post-processing. This elimination process is accomplished in two steps: first, the original SIT images are binarized, that is, the binary value is 1 for bubble and 0 for nonbubble; then, the tracer particle positions obtained by the PMC method are collated with the binary data. When the binary value at the tracer particle position is 1, it is defined as particle overlapping on a bubble shadow and is then eliminated.

The velocity vectors of the liquid phase and bubbles are accurately detected after the abovementioned data-processing procedures, so that the characteristics of turbulence in a channel flow modified by microbubbles injection and the bubble–turbulence interactions are able to be explored statistically (Kitagawa et al., 2005).

Lindken and Merzkirch (2002) also reported a measurement technique for two-phase bubbly flows using the combination of PIV/LIF/SIT, in which only one CCD camera is used for recording both PIV/LIF and SIT images. Nd:YAG laser at 532 nm wavelength is used to illuminate a 2D light sheet in the bubbly flow. The emit light from the applied fluorescent tracer particles has a wavelength of 555–585 nm with an emission peak at 566 nm. The LED array for SIT emits light at 675 nm. An optical high pass filter with a steep transmission edge at 570 nm $\pm$ 5 nm is then used to completely block the reflected light at 532 nm, whereas the shadow image with light of wavelength 675 nm and most of the fluorescent light passes the filter and are imaged by the same CCD camera. Thus, both information of liquid-phase velocity field and the gas bubble's shape and position can be determined by properly designed algorithms. In an experimental study on single bubble dynamics in a small diameter pipe (Hassan et al., 2001), stereoscopic PIV combined with SIT, without LIF, however, are used as the measurement approaches. The recording system consists of four CCD cameras. One camera together with optical filter records SIT images in the direction parallel to the laser sheet; one camera is set perpendicular to the laser sheet for PIV and records PIV images for analysis of bubble information together with the SIT images. The other two cameras are for stereoscopic PIV images recording. The centroid, rotation angle, and semiaxes of the ellipse that best fits the edge points of the bubble image are computed using the direct generalized Hough transform algorithm, which only applied to images from the orthogonally positioned cameras. In this way, the velocity field generated by the passage of a single air bubble rising in quiescent water in conjunction with the bubble size and shape can be obtained simultaneously.

4.2.3 Gas–liquid two-phase flows in microchannels

Research topics on gas–liquid two-phase flows in microchannels are receiving increasing notice recently due to its importance in such areas as two-phase microchannel heat sinks, identification of micro-scaled

two-phase regime, multiphase microfluidics, etc. Experiments on gas–liquid two-phase microchannel flows using PIV technique (μ-PIV) may not encounter sever difficulty resulted from the strong reflection of illumination light from the gas–liquid interface, as possibly happens to a PIV (only) measurement of gas–liquid two-phase flow in a normal-sized geometry, since LIF technique is actually always utilized to any μ-PIV system, either a normal μ-PIV or a confocal PIV system. The data-processing procedure is thus relatively simple. Only two examples of PIV techniques used for measurement of gas–liquid two-phase flows in microchannels are described as follows.

Wang et al. (2006) reported a hybrid experimental and computational method for reconstructing 3D bubble geometry as well as providing other critical information associated with nucleating bubbles in gas–liquid two-phase microchannel flows. A normal μ-PIV system is used to measure the water phase 2D-2C velocity field surrounding a nucleating bubble. This 2D-2C velocity field locates in a 2D slice of the 3D flow. To yield the 3D flow field as well as bubble geometry, a variety of 3D flow solutions for bubbles with varying diameters and center locations but identical bubble cross-sections are then numerically predicted, and then the in-plane projection of the predicted 3D velocity vectors at the focal plane are compared to the respective μ-PIV measurements; finally, the best match between the predicted and μ-PIV-measured velocity fields gives an estimate of the actual bubble geometry (Wang et al., 2006). In the μ-PIV study of the formation of segmented flow in microfluid T-junctions (Van Steijn et al., 2007), the digital mask technique is utilized to eliminate spurious vectors due to background noise in the gas phase. To build up a mask, the so-called Q-ratio, that is, the ratio between the largest and second-largest peak in the correlation field of PIV images is computed, resulting in grayscale images. These images are then binarized and used as a mask for the PIV vector fields. The shape and movement of the interface between the liquid and gas phases are measured by means of a high-speed camera. Hence, the characteristics of such transient flow field during the formation of bubbles in a microfluidic T-junction can be investigated.

4.3 Particle-laden multiphase flows

Particle-laden multiphase flows, usually turbulent, cover a wide range of applications, such as pollution control, sediment transport, combustion processes, erosion effects in gas turbines, and so on. One of the most important aspects of particle-laden turbulent flows is the mutual interactions between particles and turbulence. PIV techniques, as a powerful tool other than numerical simulation method and theoretical analysis, have been applied to this research field of particle-laden multiphase flows. Note that, dispersed-phase particles in particle-laden

multiphase flows usually do not refer to the seeding particles for PIV, the former are normally much larger than the latter. In the PIV investigation of particle-laden multiphase flows, the key issue is to not only measure velocity field in the continuous phase, but also distinguish the dispersed particles or droplets from its environment and detect the dispersed particle path location within the illuminating laser sheet. Several typical examples of treatment method for PIV measurement of particle-laden multiphase flows are described later.

In an experimental study on a downward particle-laden water channel flow by Sato and Hishida (1996), a special function for particle-laden two-phase flows is supplemented to the conventional PIV system: a two-control volume method comprising an Ar-laser sheet and two infrared laser diode sheets located along both sides of the Ar-laser sheet is used. In this way, the dispersed particles are correctly recognized and its velocities and water-phase velocity field are obtained simultaneously, so that the interactions between dispersed particles and fluid turbulence have been studied (Sato and Hishida, 1996). A further study of the effect of inter-particle spacing on turbulence modulation in a downward particle-laden water channel flow is carried out by Sato et al. (2000) using a Lagrangian PIV technique. A high-speed CCD camera for recording PIV images and a cylindrical lens for introducing a laser sheet to the flow field to be investigated are mounted on a moving shuttle, which moves from top to the bottom, parallel to the water channel wall, with mean streamwise velocity of the laden particles on which it focuses, to realize the Lagrangian measurement technique. By using the PIV technique combined with the moving shuttle, it is possible to measure the Lagrangian velocity field following some targeted particles, so that the distortion of turbulence in the presence of particles and the small-scale structure of turbulence modulation in terms of the inter-particle spacing can be investigated.

Kiger and Pan (2000) reported a PIV technique for the simultaneous measurement of dilute solid–liquid two-phase flows, in which a 2D median filter is employed to separate the larger dispersed phase particle image from the continuous phase tracer particle image. This phase separation technique is based on two aspects that a median filter is a nonlinear signal processing technique that has been found effective in reducing random noise and periodic interference patterns without severely degrading the signal, and that for a two-phase image with both small tracer particles for PIV and large dispersed particles, the small tracer particles can be regarded as noise scattered over a uniform background. After phase separation, the velocity vectors of the dispersed large particles are then calculated using a correlation tracking algorithm and the velocity field of the continuous phase is estimated through a standard cross-correlation-based method (Kiger and Pan, 2000).

Borowsky and Wei (2007) proposed a hybrid PIV/LIF/PIA (particle image accelerometry) technique to measure the kinematic and dynamic parameters of a liquid–solid pipe flow. In this technique, two CCD cameras are utilized and positioned 180° apart such that both focuses on the same briefly illuminated region of flow passing vertically through the transparent tube test section made of acrylic resin. The dispersed phase solid particles are silver-coated glass spheres and the seeding particles for PIV are fluorescent acrylic particles. Optical filters are employed to each camera so that the cameras recorded the trajectories of either the solid particles for PIA or the neutrally buoyant fluorescent fluid tracer particles for PIV. Simultaneous two-color PIV/PIA measurements are then realized. Both velocity and acceleration fields are calculated using the correlation-based PIV algorithm. The kinematic terms and dynamic parameters as the second and third central moments of temporal acceleration for both water and solid phases are then investigated.

PIV techniques have also been applied to the measurement of gas–liquid–solid three-phase flows. Chen and Fan (1992) and Chen et al. (1994) applied a 2D PIV system to simultaneously measure the instantaneous full-field flow properties of all components in a gas–liquid and gas–liquid–solid fluidization system. Reese et al. (1995) extend the 2D PIV system developed by Chen and Fan (1992) to a 3D PIV and measure the 3D local flow properties of three-phase fluidization systems. The three-phase flow to be investigated consists of the continuous water phase, neutrally buoyant Pliolite particles of 200–500 μm in diameter for PIV tracer particles and solid phase as well, and dispersed gas bubbles injected from the bottom of water pipe flow. The 3D PIV system consists of three major components: an Ar-CW laser with optics providing laser sheet with 1.0 cm in thickness, one CCD camera for image recording, and image-processing system. An optical arrangement using six pieces of mirror is utilized for the one-camera-based 3D PIV technique. The left and right sides (half-half) of each PIV image recorded by the only one camera with the aid of the optical arrangement contains the displacement of particles in two orthogonally different planes, respectively. The 3D PIV algorithms (and calibration procedures) are then developed to identify particle (where "particle" is used in a broad sense to include gas bubbles, solid particles, and liquid seeding particles) images, locate centroids of particle images, distinguish particle images between different phases, compute displacements between image pairs, match image pairs from the orthogonal views of the flow field, and reconstruct the 3D spatial coordinates of particle images and thus the 3D instantaneous velocities. This 3D PIV system has been applied to the 3D gas–liquid–solid fluidization system operating in the dispersed bubble flow regime and testified that it is capable of providing the 3D full-field instantaneous velocities, accelerations, and holdups (concentrations) of different phases (Reese et al., 1995).

5. SUMMARY AND OUTLOOK

The conventional 2D PIV technique has almost matured and become a standard nonintrusive diagnostic tool of flow measurement. 3D PIV measurement, which can achieve the most comprehensive information of the flow characteristics to be studied, is usually either difficult to accomplish or expensive, motivating experimentalists to develop more and more convenient, inexpensive and robust 3D PIV techniques. Indeed, several techniques such as the 3D μ-PIV, particularly for highly unsteady flow measurement in microchannels, are still at its infant stage. The development of PIV techniques relies on the development of its hardware components as well as designing ideas of the arrangement of illumination, optics, image recording system, and the analysis algorithms.

Applications of PIV techniques, ranging from 2D-2C to 3D-3C, from parallel and orthogonal dual-plane PIV to time-resolved PIV, to the measurement of single-phase flows have obtained vast achievement in understanding the fluid dynamics at both macro and micro scales. PIV measurement of multiphase flow systems normally need to achieve additional information like the interactions between phases as well as the velocity field in the continuous phase flow. This requirement needs more skills in addition to the PIV measurement of single-phase flow, including the particularly designed data analysis methods for phase-distinguishing and estimation of velocity vectors of dispersed phase(s), and sometime additional measurement techniques such as LIF and SIT. It is reasonable to comment that, with careful and detailed considerations, PIV techniques are generally applicable to the measurement of multiphase flow systems as far as the PIV measurement can be performed on a single-phase flow flowing in the same environment, but lots of know-how is necessary for these additional considerations.

The essence of PIV (including PTV) technique, that is, yielding the velocity vectors from analyses of the viewed and recorded image patterns, can be quoted to establish novel estimation techniques for wider field of researches. The estimation of velocity distribution of the floating ice pieces on a river based on PIV algorithm is one of the best examples (Ettema et al., 1997). Freeing one's imagination, the multiphase flow systems can also be extended to a much broader scope, which may involve, for example, cherry-blossom petals falling down in the wind, clouds floating in the sky, a group of snow finches flying in the air, rocks or other solid pieces rolling with the earthquake or heavy rain-induced landslide, pollution materials floating and collecting at the water surface, cars running in a big city, and so on. PIV algorithms are suitable to estimate those movement behaviors as far as the viewed and recorded

scope can be large enough to cover them. PIV might be able to measure the flowing or moving or floating velocities for everything in the imagination of human beings, which, on the other hand, requires the endless development of this technique.

NOTATION

A	area of the investigated object
C_{fg}	cross-correlation function
d_0	diameter of laser beam
f	variable extracted from the PIV image
f_m	average value of f
g	variable extracted from the PIV image
g_m	average value of g
H	height of flow channel
I	image intensity
i	ith location
j	jth location
L	circumference length of the investigated object
N	pixel number in one direction of an interrogation window
n	counted number
$\tilde{p}(x_i, y_j)$	local standard deviation of the contrast intensity of an image
R_{fg}	cross-correlation coefficient
$T_{\tilde{p}}$	a threshold limiting the value of $\tilde{p}(x_i, y_j)$
$T_{\Delta y}$	A threshold limiting the spreading distance of the peak of $\tilde{p}(x_i, y_j)$ in the y direction
t	time
u	velocity component in the x direction
$\vec{u}_{i,j}$	velocity vector at grid (i, j)
x	x component in the Cartesian coordinate
y	y component in the Cartesian coordinate
z	z component in the Cartesian coordinate
Δx	sample shift in the x direction
Δy	sample shift in the y direction

GREEK LETTERS

δ_m	minimum thickness of laser sheet
λ	wavelength of laser light
π	ration of the circumference of a circle to its diameter

ABBREVIATIONS

2D-2C	two-dimensional two-component
2D-3C	two-dimensional three-component
3D-3C	three-dimensional three-component
CCD	charge-coupled device
CFD	computational fluid dynamics
CMOS	complementary metal-oxide semiconductor
CW	continuous wave
DPIV	defocusing particle image velocimetry
GLCM	gray-level co-occurrence matrix
HPIV	holographic particle image velocimetry
LFCPIV	local-field correlation particle image velocimetry
LIF	laser-induced fluorescence
NA	numerical aperture
PDMS	polydimethylsiloxane
PIA	particle image accelerometer
PIV	particle image velocimetry
PLIF	planar laser-induced fluorescence
PMC	particle mask correlation
PTV	particle tracking velocimetry
SIT	shadow image technique
TPIV	tomographic particle image velocimetry
VGT	velocity gradient tensor
WIDIM	window displacement iterative multigrid
μ-PIV	micro-scaled particle image velocimetry
μ-DPIV	micro-scaled defocusing particle image velocimetry
μ-HPIV	micro-scaled holographic particle image velocimetry

REFERENCES

Adrian, R. J. *Appl. Opt.* **23**, 1690–1691 (1984).
Adrian, R. J. *Annu. Rev. Fluid Mech.* **23**, 261–304 (1991).
Adrian, R. J. *Meas. Sci. Technol.* **8**, 1393–1398 (1997).
Adrian, R. J. *Exp. Fluids* **39**, 159–169 (2005).
Adrian, R. J. *Phys. Fluids* **19**, 041301 (2007).
Adrian, R. J., Christensen, K. T., and Liu, Z.-C. *Exp. Fluids* **29**, 275–290 (2000a).
Adrian, R. J., Meinhart, C. D., and Tomkins, C. D. *J. Fluid Mech.* **422**, 1–54 (2000b).
Afanasyev, Y. D., and Demirov, E. K. *Exp. Fluids* **39**, 828–835 (2005).
Akedo, Y., Oshima, M., Oishi, M., and Saga, T.,"Visualization of flow structure in cerebral aneurysm model", The 8th Asian Symposium on Visualization, Chiangmai, Thailand, ID46 (2005).
Angele, K. P., Suzuki, Y., Miwa, J., and Kasagi, N. *Meas. Sci. Technol.* **17**, 1639–1646 (2006).
Arroyo, M. P., and Greated, C. A. *Meas. Sci. Technol.* **2**, 1181–1186 (1991).
Balakumar, B. J., and Adrian, R. J. *Exp. Fluids* **36**, 166–175 (2004).

Bastiaans, R. J. M., Plas, G. A. J., and Kieft, R. N. *Exp. Fluids* **32**, 346–356 (2002).
Bi, W. T., Sugii, Y., Okamoto, K., and Madarame, H. *Meas. Sci. Technol.* **14**, L1–L5 (2003).
Borowsky, J., and Wei, T. *ASME J. Fluid Eng.* **129**, 1415–1421 (2007).
Bourdon, C. J., Olsen, M. G., and Gorby, A. D. *Exp. Fluids* **37**, 263–271 (2004a).
Bourdon, C. J., Olsen, M. G., and Gorby, A. D. *Meas. Sci. Technol.* **15**, 318–327 (2004b).
Bown, M. R., MacInnes, J. M., and Allen, R. W. K. *Exp. Fluids* **42**, 197–205 (2007).
Bown, M. R., MacInnes, J. M., Allen, R. W. K., and Zimmerman, W. B. J. *Meas. Sci. Technol.* **17**, 2175–2185 (2006).
Broder, D., and Sommerfeld, M. *Exp. Fluids* **33**, 826–837 (2002).
Brucker, C. *Meas. Sci. Technol.* **8**, 1480–1492 (1997).
Burgmann, S., Brucker, C., and Schroder, W. *Exp. Fluids* **41**, 319–326 (2006).
Burgmann, S., Dannemann, J., and Schroder, W. *Exp. Fluids* **44**, 609–622 (2008).
Carlier, J., and Stanislas, M. *J. Fluid Mech.* **535**, 143–188 (2005).
Chen, R. C., and Fan, L.-S. *Chem. Eng. Sci.* **47**, 3615–3622 (1992).
Chen, J., and Katz, J. *Meas. Sci. Technol.* **16**, 1605–1618 (2005).
Chen, R. C., Reese, J., and Fan, L.-S. *AIChE. J.* **40**(1093), 1104 (1994).
Christensen, K. T. *Exp. Fluids* **36**, 484–497 (2004).
Christensen, K. T., and Adrian, R. J. J. *Fluid Mech.* **431**, 433–443 (2001).
Coudert, S. J. M., and Schon, J. P. *Meas. Sci. Technol.* **12**, 1371–1381 (2001).
Coupland, J. M., Garner, C. P., Alcock, R. D., and Halliwell, N. A. J. *Phys. Conf. Ser.* **45**, 29–37 (2006).
Deen, N. G., Westerweel, J., and Delnoij, E. *Chem. Eng. Technol.* **25**, 97–101 (2002).
Deng, R.-S., and Wang, C.-H. *Phys. Fluids* **15**, 3718–3729 (2003).
Diez, F. J., Bernal, L. P., and Faeth, G. M. *Int. J. Heat Fluid Flow* **26**, 873–882 (2005).
Elsinga, G. E., Scarano, F., Wieneke, B., and Van Oudheusden, B. W. *Exp. Fluids* **41**, 933–947 (2006a).
Elsinga, G. E., Van Oudheusden, B. W., and Scarano, F., Experimental assessment of tomographic-PIV accuracy, Proceedings of the 13th International Symposium Application of Laser Techniques to Fluid Mechanics, Lisbon, Portugal (2006b).
Ettema, R., Fujita, I., Muste, M., and Kruger, A. *Cold Reg. Sci. Technol.* **26**, 97–112 (1997).
Fincham, A. M., and Delerce, G. *Exp. Fluids* **29**, S13–S22 (2000).
Fincham, A. M., and Spedding, G. R. *Exp. Fluids* **23**, 449–462 (1997).
Fore, L. B., Tung, A. T., Buchanan, J. R., and Welch, J. W. *Exp. Fluids* **39**, 22–31 (2005).
Fouras, A., Dusting, J., and Hourigan, K. *Exp. Fluids* **42**, 799–819 (2007).
Fouras, A., Jacono, D. L., and Hourigan, K. *Exp. Fluids* **44**, 317–329 (2008).
Fujiwara, A., Danmoto, Y., Hishida, K., and Maeda, M. *Exp. Fluids* **36**, 157–165 (2004a).
Fujiwara, A., Minato, D., and Hishida, K. *Int. J. Heat Fluid Flow* **25**, 481–488 (2004b).
Ganapathisubramani, B. *Phys. Fluids* **19**, 098108 (2007).
Ganapathisubramani, B., Clemens, N. T., and Dolling, D. S. *J. Fluid Mech.* **556**, 271–282 (2006a).
Ganapathisubramani, B., Hutchins, N., Hambleton, W. T., Longmire, E. K., and Marusic, I. *J. Fluid Mech.* **524**, 57–80 (2005b).
Ganapathisubramani, B., Longmire, E. K., and Marusic, I. *J. Fluid Mech.* **478**, 35–46 (2003).
Ganapathisubramani, B., Longmire, E. K., and Marusic, I. *Phys. Fluids* **18**, 055105 (2006b).
Ganapathisubramani, B., Longmire, E. K., Marusic, I., and Pothos, S. *Exp. Fluids* **39**, 222–231 (2005a).
Gaydon, M., Raffel, M., Willert, C., Rosengarten, M., and Kompenhans, J. *Exp. Fluids* **23**, 331–334 (1997).
Grant, I., Fu, S., Pan, X., and Wang, X. *Exp. Fluids* **19**, 214–221 (1995).
Gui, L., and Merzkirch, W. *Exp. Fluids (Suppl.)* S465–S468 (1996).
Gui, L., Merzkirch, W., and Fei, R. *Exp. Fluids* **29**, 30–35 (2000).
Gui, L., and Wereley, S. T. *Exp. Fluids* **32**, 506–517 (2002).

Gunther, A., Jhunjhunwala, M., Thalmann, M., Schmidt, M. A., and Jensen, K. F. *Langmuir* **21**, 1547–1555 (2005).
Hambleton, W. T., Hutchins, N., and Marusic, I. *J. Fluid Mech.* **560**, 53–64 (2006).
Harada, K., Murakami, M., and Ishii, T. *Cryogenics* **46**, 648–657 (2006).
Hart, D. P. *J. Vis.* **3**, 187–194 (2000a).
Hart, D. P. *Exp. Fluids* **29**, 13–22 (2000b).
Hassan, Y. A., Ortiz-Villafuerte, J., and Schmidl, W. D. *Int. J. Multiphase Flow* **27**, 817–842 (2001).
Hassan, Y. A., Schmidl, W., and Ortiz-Villafuerte, J. *Meas. Sci. Technol.* **9**, 309–326 (1998).
Herrmann, S. F., Hinrichs, H., Hinsch, K. D., and Surmann, C. *Exp. Fluids* **29**, S108–S116 (2000).
Herrmann, S. F., and Hinsch, K. D. *Meas. Sci. Technol.* **15**, 613–621 (2004).
Hinsch, K. D. *Meas. Sci. Technol.* **6**, 742–753 (1995).
Hinsch, K. D. *Meas. Sci. Tecnnol.* **13**, R61–R72 (2002).
Hori, T., and Sakakibara, J. *Meas. Sci. Technol.* **15**, 1067–1078 (2004).
Hou, Y. X., Somandepalli, V. S. R., and Mungal, M. G. *J. Fluid Mech.* **597**, 31–66 (2008).
Hu, H., Saga, T., Kobayashi, T., and Taniguchi, N. *Phys. Fluids* **14**, 2128–2138 (2002).
Hu, H., Saga, T., Kobayashi, T., Taniguchi, N., and Yasuki, M. *Exp. Fluids* **31**, 277–293 (2001).
Huang, H. *Exp. Fluids* **24**, 364–372 (1998).
Huang, H., Dabiri, D., and Gharib, M. *Meas. Sci. Technol.* **8**, 1427–1440 (1997).
Huang, H. T., Fiedler, H. E., and Wang, J. J. *Exp. Fluids* **15**, 263–273 (1993).
Hutchins, N., Hambleton, W. T., and Marusic, I. *J. Fluid Mech.* **541**, 21–54 (2005).
Ishikawa, M., Murai, Y., Wada, A., Iguchi, M., Okamoto, K., and Yamamoto, F. *Exp. Fluids* **29**, 519–531 (2000).
Jambunathan, K., Ju, X. Y., Dobbins, B. N., and Ashforth-Frost, S. *Meas. Sci. Technol.* 6, 507, 514 (1995).
Jeon, D., Pereira, F., and Gharib, M. *Part. Part. Syst. Charact.* **20**, 193–198 (2003).
Kahler, C. J. *Exp. Fluids* **36**, 114–130 (2004).
Kahler, C. J., and Kompenhans, J., Multiple plane stereo PIV: Technical realization and fluid-mechanical significance. Proceedings of the 3rd International Workshop on Particle Image Velocimetry, Santa Barbara, CA, USA (1999).
Kahler, C. J., and Kompenhans, J. *Exp. Fluids (Suppl.)* S70–S77 (2000).
Kajitani, L., and Dabiri, D. *Meas. Sci. Technol.* **16**, 790–804 (2005).
Kashid, M. N., Gerlach, I., Goetz, S., Franzke, J., Acker, J. F., Platte, F., Agar, D. W., and Turek, S. *Ind. Eng. Chem. Res.* **44**, 5003–5010 (2005).
Keane, R. D., and Adrian, R. J. *Meas. Sci. Technol.* **1**, 1202–1215 (1990).
Keane, R. D., and Adrian, R. *J. Appl. Sci. Res.* **49**, 191–215 (1992).
Keane, R. D., Adrian, R. J., and Zhang, Y. *Meas. Sci. Technol.* **6**, 754–768 (1995).
Kiger, K. T., and Pan, C. *ASME J. Fluids Eng.* **122**, 811–818 (2000).
Kim, K. C., Yoon, S. Y., Kim, S. M., Chun, H. H., and Lee, I. *Exp. Fluids* **40**, 876–883 (2006).
Kinoshita, H., Kaneda, S., Fujii, T., and Oshima, M. *Lab Chip* **7**, 338–346 (2007).
Kitagawa, A., Hishida, K., and Kodama, Y. *Exp. Fluids* **38**, 466–475 (2005).
Kumar, S., and Banerjee, S. *Phys. Fluids* **10**, 160–177 (1998).
Lawson, N. J., and Wu, J. *Meas. Sci. Technol.* **8**, 1455–1464 (1997).
Lecordier, B., Demare, D., and Vervisch, L. M. J. *Meas. Sci. Technol.* **12**, 1382–1391 (2001).
Li, F.-C., Kawaguchi, Y., Hishida, K., and Oshima, M. *Exp. Fluids* **40**, 218–230 (2006a).
Li, F.-C., Kawaguchi, Y., Segawa, T., and Hishida, K. *Phys. Fluids* **17**, 075104 (2005a).
Li, F.-C., Kawaguchi, Y., Segawa, T., and Hishida, K. *Chin. Phys. Lett.* **22**, 624–627 (2005b).
Li, F.-C., Kawaguchi, Y., Segawa, T., and Suga, K. *Exp. Fluids* **39**, 945–953 (2005c).
Li, F.-C., Kawaguchi, Y., Segawa, T., and Suga, K. *Phys. Fluids* **17**, 082101 (2005d).
Li, F.-C., Kawaguchi, Y., Segawa, T., and Hishida, K. *Chin. Phys. Lett.* **23**, 1226–1229 (2006b).

Li, F.-C., Oishi, M., Kawaguchi, Y., Oshima, N., and Oshima, M., Experimental study of swirling flow of a viscoelastic fluid with deformed free surface, Proceedings of the ASME Joint U.S.–European Fluids Engineering Summer Meeting, July 17–20, Miami, FL, USA, Paper No. FEDSM2006-98387 (2006c).
Li, F.-C., Oishi, M., Oshima, N., Kawaguchi, Y., and Oshima, M., Statistical characteristics of elastic turbulence in a free-surface swirling flow, New Trends in Fluid Mechanics Research, Proceedings of the 5th International Conference on Fluid Mechanics, Shanghai, China, August 15–19, pp. 91–94, Tsinghua University Press and Springer (2007).
Li, F.-C., Yu, B., Wei, J.-J., Kawaguchi, Y., and Hishida, K. *Int. J. Heat Mass Transfer* **51**, 835–843 (2008).
Liao, Q., and Cowen, E. A. *Exp. Fluids* **38**, 197–208 (2005).
Liberzon, A., Gurka, R., and Hetsroni, G. *Exp. Fluids* **36**, 355–362 (2003).
Lima, R., Wada, S., Takeda, M., Tsubota, K., and Yamaguchi, T. *J. Biomech.* **40**, 2752–2757 (2007).
Lima, R., Wada, S., Tanaka, S., Takeda, M., Ishikawa, T., Tsubota, K., Imai, Y., and Yamaguchi, T. *Biomed. Microdevices* **10**, 153–167 (2008).
Lima, R., Wada, S., Tsubota, K., and Yamaguchi, T. *Meas. Sci. Technol.* **17**, 797–808 (2006).
Lindken, R., Gui, L.-C., and Merzkirch, W. *Chem. Eng. Technol.* **22**, 202–206 (1999).
Lindken, R., and Merzkirch, W. *Exp. Fluids (Suppl.)* S194–S201 (2000).
Lindken, R., and Merzkirch, W. *Exp. Fluids* **33**, 814–825 (2002).
Lindken, R., Westerweel, J., and Wieneke, B. *Exp. Fluids* **41**, 161–171 (2006).
Liu, Z., Adrian, R. J., and Hanratty, T. J. J. *Fluid Mech.* **448**, 53–80 (2001).
Liu, Z.-L., Jia, L.-F., Zheng, Y., and Zhang, Q.-K. *Chem. Eng. Sci.* **60**, 3537–3552 (2005).
Liu, Z.-L., Jia, L.-F., Zheng, Y., and Zhang, Q.-K. *Chem. Eng. Sci.* **63**, 1–11 (2008).
Lobera, L., and Coupland, J. M. *Meas. Sci. Technol.* **19**, 025501 (2008).
Longmire, E. K., Ganapathisubramani, B., Marusic, I., Urness, T., and Interrante, V. J. *Turbulence* **4**, 023 (2003).
Lueptow, R. M., Akonur, A., and Shinbrot, T. *Exp. Fluids* **28**, 183–186 (2000).
Maas, H. G., Gruen, A., and Papantoniou, D. *Exp. Fluids* **15**, 133–146 (1993).
Malsch, D., Kielpinski, M., Merthan, R., Albert, J., Mayer, G., Kohler, J. M., Susse, H., Stahl, M., and Henkel, T. *Chem. Eng. J.* **135S**, S166–S172 (2008).
McKenna, S. P., and McGillis, W. R. *Exp. Fluids* **32**, 106–115 (2002).
Meinhart, C. D., Wereley, S. T., and Gray, H. B. *Meas. Sci. Technol.* **11**, 809–814 (2000).
Melling, A. *Meas. Sci. Technol.* **8**, 1406–1416 (1997).
Meng, H., Pan, G., Pu, Y., and Woodward, S. H. *Meas. Sci. Technol.* **15**, 673–685 (2004).
Mielnik, M. M., and Saetran, L. R. *Exp. Fluids* **41**, 155–159 (2006).
Misra, S. K., Thomas, M., Kambhamettu, C., Kirby, J. T., Veron, F., and Brocchini, M. *Exp. Fluids* **40**, 764–775 (2006).
Mullin, J. A., and Dahm, W. J. A. *Exp. Fluids* **38**, 185–196 (2005).
Mullin, J. A., and Dahm, W. J. A. *Phys. Fluids* **18**, 035101 (2006a).
Mullin, J. A., and Dahm, W. J. A. *Phys. Fluids* **18**, 035102 (2006b).
Natrajan, V. K., Wu, Y., and Christensen, K. T. *J. Fluid Mech.* **574**, 155–167 (2007).
Nogueira, J., Lecuona, A., and Rodriguez, P. A. *Exp. Fluids* **27**, 107–116 (1999).
Nogueira, J., Lecuona, A., and Rodriguez, P. A. *Meas. Sci. Technol.* **12**, 1911–1921 (2001a).
Nogueira, J., Lecuona, A., and Rodriguez, P. A. *Exp. Fluids* **30**, 309–316 (2001b).
Nogueira, J., Lecuona, A., and Rodriguez, P. A. *Exp. Fluids* **39**, 305–313 (2005a).
Nogueira, J., Lecuona, A., and Rodriguez, P. A. *Exp. Fluids* **39**, 314–321 (2005b).
Olsen, M. G., and Adrian, R. J. *Exp. Fluids* **29**, S166–S174 (2000a).
Olsen, M. G., and Adrian, R. J. *Opt. Laser Technol.* **32**, 621–627 (2000b).
Olsen, M. G., and Bourdon, C. J. *J. Fluids Eng.* **125**, 895–901 (2003).
Ooms, T., Koek, W., Braat, J., and Westerweel, J. *Meas. Sci. Technol.* **17**, 304–312 (2006).

Ooms, T., Koek, W., and Westerweel, J. *Meas. Sci. Technol.* **19**, 074003 (2008).
Ostendorf, M., and Schwedes, J. *Powder Technol.* **158**, 69–75 (2005).
Park, J. S., Choi, C. K., and Kihm, K. D. *Exp. Fluids* **37**, 105–119 (2004).
Park, J. S., and Kihm, K. D. *Opt. Lasers Eng.* **44**, 208–223 (2006).
Pereira, F., and Gharib, M. *Meas. Sci. Technol.* **13**, 683–694 (2002).
Pereira, F., Gharib, M., Dabiri, D., and Modarress, D. *Exp. Fluids (Suppl.)* S78–S84 (2000).
Pereira, F., Lu, J., Castano-Graff, E., and Gharib, M. *Exp. Fluids* **42**, 589–599 (2007).
Philip, O. G., Schmidl, W. D., and Hassan, Y. A. *Nucl. Eng. Des.* **149**, 375–385 (1994).
Pickering, C. J. D., and Halliwell, N. *Appl. Opt.* **23**, 2961–2969 (1984).
Prasad, A. K. *Exp. Fluids* **29**, 103–116 (2000).
Prasad, A. K., and Jensen, K. *Appl. Opt.* **34**, 7092–7099 (1995).
Pu, Y., and Meng, H. *Exp. Fluids* **29**, 184–197 (2000).
Raffel, M., Willert, C. E., Werely, S. T., and Kompenhans, J., "Particle Image Velocimetry: A Practical Guide". 2nd Ed. Springer, Berlin (2007).
Reese, J., Chen, R. C., and Fan, L.-S. *Exp. Fluids* **19**, 367–378 (1995).
Reul, N., Branger, H., and Giovanageli, J. P. *Phys. Fluids* **11**, 1959–1961 (1999).
Reul, N., Branger, H., and Giovanageli, J. P. *Boundary Layer Meteorology* **126**, 477–505 (2008).
Roesgen, T. *Exp. Fluids* **35**, 252–256 (2003).
Rohaly, J., Frigerio, F., and Hart, D. P. *Meas. Sci. Technol.* **13**, 984–996 (2002).
Royer, H. *Meas. Sci. Technol.* **8**, 1562–1572 (1997).
Santiago, J. G., Wereley, S. T., Meinhart, C. D., Beebe, D. J., and Adrian, R. J. *Exp. Fluids* **25**, 316–319 (1998).
Sarrazin, F., Loubiere, K., Prat, L., Gourdon, C., Bonometti, T., and Magnaudet, J. *AIChE J.* **52**, 4061–4069 (2006).
Sato, Y., Fukuichi, U., and Hishida, K. *Int. J. Heat Fluid Flow* **21**, 554–561 (2000).
Sato, Y., and Hishida, K. *Int. J. Heat Fluid Flow* **17**, 202–210 (1996).
Sato, Y., Irisawa, G., Ishizuka, M., Hishida, K., and Maeda, M. *Meas. Sci. Technol.* **14**, 114–121 (2003).
Scarano, F. *Meas. Sci. Technol.* **13**, R1–R9 (2002).
Scarano, F. *Meas. Sci. Technol.* **15**, 475–486 (2004).
Scarano, F., and Riethmuller, M. L. *Exp. Fluids* **26**, 513–523 (1999).
Scarano, F., and Riethmuller, M. L. *Exp. Fluids (Suppl.)* S51–S60 (2000).
Schroder, A., Geisler, R., Elsinga, G. E., Scarano, F., and Dierksheide, U. *Exp. Fluids* **44**, 305–316 (2008).
Shaikh, N., and Siddiqui, K. *Ocean Dyn.* **58**, 65–79 (2008).
Shinohara, K., Sugii, Y., Aota, A., Hibara, A., Tokeshi, M., Kitamori, T., and Okamoto, K. *Meas. Sci. Technol.* **15**, 1965–1970 (2004).
Shinohara, K., Sugii, Y., Jeong, J. H., and Okamoto, K. *Rev. Sci. Instrum.* **76**, 106109 (2005).
Sielamowicz, I., Blonski, S., and Kowalewski, T. A. *Chem. Eng. Sci.* **60**, 589–598 (2005).
Soloff, S. M., Adrian, R. J., and Liu, Z.-C. *Meas. Sci. Technol.* **8**, 1441–1454 (1997).
Soria, J. *Exp. Therm. Fluid Sci.* **12**, 221–233 (1996).
Spedding, G. R., and Rignot, E. J. M. *Exp. Fluids* **15**, 417–430 (1993).
Stamhuis, E. J. *Aquatic Ecol.* **40**, 463–479 (2006).
Steijn, V., Kreutzer, M. T., and Kleijn, C. R. *Chem. Eng. Sci.* **62**, 7505–7514 (2007).
Steingart, D. A., and Evans, J. W. *Chem. Eng. Sci.* **60**, 1043–1051 (2005).
Stitou, A., and Riethmuller, M. L. *Meas. Sci. Technol.* **12**, 1398–1403 (2001).
Sugii, Y., Okuda, R., Okamoto, K., and Madarame, H. *Meas. Sci. Technol.* **16**, 1126–1130 (2005).
Susset, A., Most, J. M., and Honore, D. *Exp. Fluids* **40**, 70–79 (2006).
Svizher, A., and Cohen, J. *Exp. Fluids* **40**, 708–722 (2006a).
Svizher, A., and Cohen, J. *Phys. Fluids* **18**, 014105 (2006b).
Takehara, K., and Etoh, T. *J. Visual* **1**, 313–323 (1999).
Tao, B., Katz, J., and Meneveau, C. *Phys. Fluids* **12**, 941–944 (2000).

Tao, B., Katz, J., and Meneveau, C. *J. Fluid Mech.* **457**, 35–78 (2002).
Theunissen, R., Scarano, F., and Riethmuller, M. L. *Meas. Sci. Technol.* **18**, 275–287 (2007).
Tokuhiro, A., Fujiwara, A., Hishida, K., and Maeda, M. *ASME J. Fluids Eng.* **121**, 191–197 (1999).
Tokuhiro, A., Maekawa, M., Iizuka, K., Hishida, K., and Maeda, M. *Int. J. Multiphase Flow* **24**, 1383–1406 (1998).
Tomkins, C. D., and Adrian, R. J. J. *Fluid Mech.* **490**, 37–74 (2003).
Triep, M., Brucker, Ch., and Schroder, W. *Exp. Fluids* **39**, 232–245 (2005).
Van der Bos, F., Tao, B., Meneveau, C., and Katz, J. *Phys. Fluids* **14**, 2456–2474 (2002).
Van Sciver, S. W., Fuzier, S., and Xu, T. *J. Low Temp. Phys.* **148**, 225–233 (2007).
Wang, E. N., Devasenathipathy, S., Lin, H., Hidrovo, C. H., Santiago, J. G., Goodson, K. E., and Kenny, T. W. *Exp. Fluids* **40**, 847–858 (2006).
Warholic, M. D., Heist, D. K., Katcher, M., and Hanratty, T. J. *Exp. Fluids* **31**, 474–483 (2001).
Wernet, M. P. *Exp. Fluids* **28**, 97–115 (2000).
Westerweel, J. *Exp. Fluids* **16**, 236–247 (1994).
Westerweel, J. *Meas. Sci. Technol.* **8**, 1379–1392 (1997).
Westerweel, J., Dabiri, D., and Gharib, M. *Exp. Fluids* **23**, 20–28 (1997).
White, C. M., Somandepalli, V. S. R., and Mungal, M. G. *Exp. Fluids* **36**, 62–69 (2004).
Wieneke, B. *Exp. Fluids* **39**, 267–280 (2005).
Willert, C. E., and Gharib, M. *Exp. Fluids* **10**, 181–193 (1991).
Willert, C. E., and Gharib, M. *Exp. Fluids* **12**, 353–358 (1992).
Yamamoto, F., Wada, A., Iguchi, M., and Ishikawa, M. *J. Flow Visual Image Proc.* **3**, 65–78 (1996).
Yang, H., Halliwell, N. A., and Coupland, J. M., Micro holographic particle image velocimetry: Digital 3C3D measurement of free jet flow. Proceedings of the 12th International Symposium on Application of Laser Techniques to Fluid Mechanics, Lisbon, Portugal (2004).
Yoon, S. Y., and Kim, K. C. *Meas. Sci. Technol.* **17**, 2897–2905 (2006).
Zarruk, G. A. *Meas. Sci. Technol.* **16**, 1970–1975 (2005).
Zhang, J., Tao, B., and Katz, J. *Exp. Fluids* **23**, 373–381 (1997).
Zhang, T., Celik, D., and Van Sciver, S. W. *J. Low Temp. Phys.* **134**, 985–1000 (2004).
Zhang, T., and Van Sciver, S. W. *J. Low Temp. Phys.* **138**, 865–870 (2005).
Zhao, X.-L., Li, S.-Q., Liu, G.-Q., Song, Q., and Yao, Q. *Powder Technol.* **183**, 79–87 (2008).